Observations and Modeling of the Upper Mesosphere: Mesopause Characteristics, Inversion Layers, and Bores
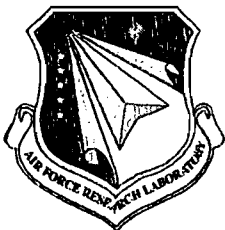
Peter P. Wintersteiner
Edward Cohen

ARCON Corporation
260 Bear Hill Road
Waltham, MA 02451-1080

AIR FORCE RESEARCH LABORATORY
Space Vehicles Directorate
29 Randolph Road
AIR FORCE MATERIEL COMMAND
Hanscom AFB, MA 01731-3010

This technical report has been reviewed and is approved for publication.

AFRL-VS-HA-TR-2005-1162

/signed/ /signed/

JEREMY WINICK ROBERT BELAND, Chief
Contract Manager Battlespace Surveillance Innovation Center

REPORT DOCUMENTATION PAGE

Form Approved
OMB No. 0704-0188

1. REPORT DATE (DD-MM-YYYY)	2. REPORT TYPE	3. DATES COVERED (From - To)
10-26-2005	Scientific Report No. 1	08-01-2004 to 07-31-2005

4. TITLE AND SUBTITLE	5a. CONTRACT NUMBER
Observations and Modeling of the Upper Mesosphere: Mesopause Characteristics, Inversion Layers, and Bores	FA8718-04-C-0031
	5b. GRANT NUMBER N/A
	5c. PROGRAM ELEMENT NUMBER 612301

6. AUTHOR(S)	5d. PROJECT NUMBER
Peter P. Wintersteiner and Edward Cohen	2301
	5e. TASK NUMBER BD
	5f. WORK UNIT NUMBER A1

7. PERFORMING ORGANIZATION NAME(S) AND ADDRESS(ES)	8. PERFORMING ORGANIZATION REPORT NUMBER
ARCON Corporation 260 Bear Hill Road Waltham, MA 02451-1080	

9. SPONSORING / MONITORING AGENCY NAME(S) AND ADDRESS(ES)	10. SPONSOR/MONITOR'S ACRONYM(S)
Air Force Research Laboratory 29 Randolph Rd. Hanscom AFB, MA 01731-3010	AFRL/VSBYM
	11. SPONSOR/MONITOR'S REPORT NUMBER(S) AFRL-VS-HA-TR-2005-1162

12. DISTRIBUTION / AVAILABILITY STATEMENT

Approved for public release; distribution unlimited.

13. SUPPLEMENTARY NOTES

14. ABSTRACT

Using data from TIMED/SABER, we studied the global behavior of the mesopause at solstice (northern-hemisphere summer). The existence of the two-level structure with an abrupt altitude transition near 25N is confirmed. Its altitude in the "summer" zone is shown to increase with increasing (northerly) latitude; in the "winter" zone, it is found somewhat below the accepted 100-km level at midlatitudes. Temperatures are in the 165-180K range throughout the winter zone but north of 25N they fall continuously, reaching ~120K at 80N. We show that mesospheric temperature inversion layers (TILs) are very common, and that large TILs affect the mesopause characteristics. We also characterize the occurrence distribution of TILs in latitude and local time.

We studied the properties of mesospheric bores by numerically solving the differential equations governing their propagation modes. Using an impulsive forcing function and measured wind and temperature profiles, we determined the vertical displacement as a function of time and horizontal distance for different altitudes within the duct, and thereby were able to study the evolution of the wave. We were able to reproduce the phase speed of an observed bore to a good approximation.

15. SUBJECT TERMS

Atmospheric radiance structure; mesospheric temperature inversion layer; MIL; TIL; SABER; global mesopause; gravity waves' ducting; mesospheric bores; Navier Stokes equations

16. SECURITY CLASSIFICATION OF:			17. LIMITATION OF ABSTRACT	18. NUMBER OF PAGES	19a. NAME OF RESPONSIBLE PERSON
a. REPORT	**b. ABSTRACT**	**c. THIS PAGE**	UU	53	Dr. Jeremy Winick
UNCLASSIFIED	UNCLASSIFIED	UNCLASSIFIED			**19b. TELEPHONE NUMBER** (include area code) 781-377-3619

Standard Form 298 (Rev. 8-98)
Prescribed by ANSI Std. Z39.18

Table of Contents

List of Figures

1. INTRODUCTION

This Interim Scientific Report describes work that was undertaken during the first twelve months that contract #FA8718-04-C-0031 was in effect. The period covered is from 1 August 2004 through 31 July 2005. The topics we discuss fall into two categories, both pertaining to the characteristics and dynamics of the upper mesosphere and their effects on the optical emissions that arise in that region.

The first category involves data from the Sounding of the Atmosphere using Broadband Emission Radiometry (SABER) instrument [*Russell et al., 1999*] on the TIMED satellite. SABER is a ten-channel radiometer that is sensitive to emissions from six important molecular constituents in the infrared (IR) and near-infrared (NIR) wavelengths. The measured radiance profiles are used to retrieve temperature and pressure, volume emission rates (VERs), and constituent mixing ratios. These and other products have been used in many studies involving the energy balance of the mesosphere and lower thermosphere (MLT), the target region for the TIMED mission. One subsection of this report deals with global characteristics of the mesopause region at solstice, as revealed by these data. Mesospheric temperature inversion layers (TILs) are treated in the other subsection. Mesospheric TILs have been observed at various locations in the past, but SABER provides the first global perspective on this subject, and reveals that they are often very large and much more common than was previously realized.

The second category involves numerical solutions of equations that govern the propagation of gravity waves within ducts in the upper mesosphere. In some circumstances, TILs provide such ducts, and thereby support the propagation of large amplitude solitary waves or internal bores, structures that are analogous to bores that have been observed in the troposphere and in tidal estuaries (rivers). Such structures propagate over great horizontal distances and, in turn, produce wavelike optical structure that has been seen in several emissions of the mesopause region. In addition to basic understanding of how they propagate, the goals are to quantify the likely range of the temperature and radiance excursions that might be seen and the rapidity with which observed radiance can be expected to vary.

2. INVESTIGATIONS OF THE MLT REGION USING SABER DATA

SABER [*Russell et al., 1999*] is a ten-channel radiometer, one of four instruments aboard the TIMED satellite. Since early in 2002, it has been continuously scanning the limb between the ground and tangent heights of approximately 300 km, recording IR and NIR emissions from CO_2, H_2O, O_3, NO, OH, and O_2.

The SABER CO_2 15 μm limb radiance is used to determine atmospheric temperature and pressure up to ~100 km. This is much higher than was previously possible, and is made possible by a new non-LTE retrieval algorithm [*Mertens et al., 2001; 2002; 2004*]. Because of good S/N ratios in the 15 μm channels, the algorithm is actually stable up to ~125 km, but the specified accuracy of three Kelvins in temperature is not achievable at those altitudes because several quantities are uncertain. Minor-constituent densities, cooling rates, and volume emission rates (VERs) are also returned for various altitude ranges in the middle atmosphere. The radiance data are referred to as Level 1B data; temperature/pressure, VERs and mixing ratios are Level 2 data.

Because of the continuous duty cycle, the high inclination of the TIMED orbit, and the sensitivity of the detectors, there is a prodigious flow of data, and near-global coverage is assured for many products up to quite high altitudes. Our studies, reported below, take advantage of this broad coverage to examine seasonal and latitudinal variations of important characteristics of the mesosphere and lower thermosphere (MLT). Among these are the principal mesopause parameters—its altitude and temperature. The global behavior of these parameters at solstice is the subject of the first subsection (2.1.). We are also studying mesospheric temperature inversion layers (TILs), which are now recognized as relatively common occurrences everywhere except in the high-latitude summer region. This is reported in the second subsection (2.2.).

In both of these cases, as in many other aspects of work on the MLT region, atmospheric tides comprise an important influence that must be accounted for. Therefore, a considerable effort has been made to distinguish the data we use according to local time (LT). We often speak of a "parameter space" consisting of season, latitude, and local time, and we have devoted some effort to extracting and sorting the retrieved temperature and measured radiance accordingly. In this context, it is important to note that the precession of the TIMED orbit is such that local times of the equator-crossings decrease by about .2 hours per day. It takes almost 60 days to view all accessible local times, between the ascending and descending portions of the orbit. The ascending/descending LT difference at the equator is about 8.8 hours. Also, times near local noon can never be observed because of detector sensitivity. Therefore, whenever the satellite precesses so the instruments point to within a certain angle close to the sun, a yaw maneuver is performed and a new ~60-day "yaw cycle" is begun.

2.1. Global Characteristics of the Mesopause at Solstice

We report here on a preliminary study of the global variability of mesopause height and temperature using SABER Level 2 (version 1.04) temperatures. This effort was concurrent with our investigation of MLT temperature-inversion layers, described below [also, *Picard et al.*, 2004; *Winick et al.*, 2004]. The layer-locating algorithm we developed for that purpose required finding the mesopause as a first step. We have concentrated on the northward-looking yaw cycle of May-July 2003 that includes the solstice (northern hemisphere summer) period. Eventually, this will be extended to a full year's worth of data.

For the current study, the mesopause has been defined as the location of the coldest temperature above the stratopause. Figure 1 shows the distribution of nighttime mesopause altitudes as a function of latitude for all SABER events between 21 June and 9 July with local time between 1 and 2 hours. The results show the low "summer" mesopause at northern high and mid-latitudes, the high "regular" mesopause extending through the winter hemisphere, and an abrupt transition between the two at ~25°N, in accord with previous observations. Figure 2 shows the altitude distribution using all of the "nighttime" data from 5 July only. Superposed upon the individual event data in Figure 2 are the mesopause altitudes calculated from mean profiles using all nighttime events—those near local midnight—in 5-degree latitude bins. Taking altitudes from the mean profiles emphasizes the sharpness of the transition. The mean altitude falls between 94 and 101 km everywhere south of the transition.

These results are generally in accord with past observations, for example those made during the *Polarstern* cruise of 1996 [*von Zahn et al., 1996*]. Those nightly-averaged measurements led to the notion of the global bipolar mesopause, at ~86 km in the mid- to high-latitude summer and ~100 km everywhere else, that is now well accepted [e.g., *Thulasiraman and Nee, 2002*]. A followup GCM model study [*Berger and von Zahn, 1999*] demonstrated that the two-level mesopause is an inherent feature of the atmosphere, not an artifact of nighttime-only measurements, and elucidated the roles of certain physical mechanisms (IR cooling, chemical heating, momentum deposition by gravity waves) that are crucial for producing it. It also showed that tides affect the mesopause altitude and temperature, but do not themselves cause the two-level phenomenon.

Although the principal characteristics of the SABER altitude distributions agree with these and other previous measurements, a more detailed picture emerges as a result of the extensive coverage and the large number of separate events that are available for study. For one thing, the spread in altitudes can be determined globally. Based on results in our figures, for instance, this spread is greater than the ~3 km originally suggested by von Zahn et al. [*1996*], especially south of the transition point. This is true even if one disregards those events for which the mesopause appears in the ~75-85 km range; those may represent anomalous circumstances, but they are common enough to require an explanation. The "regular" mesopause also appears to be lower by almost 5 km at subtropical latitudes in the winter hemisphere than at the equator and at midlatitudes. Finally, the mean altitudes shown in Figure 2, on both sides of the transition, are lower by at least 2 km than the commonly accepted altitudes of the "summer" and "regular" mesopause.

The spread of ±3 km noted above [*von Zahn et al., 1996*] represents a variation of different nights' averages at changing latitudes. It can be compared to the variation of the SABER mean altitudes given by the red squares in Figure 2, which is also approximately ±3 km. Those points, however, are centered about 97 km rather than 100 km. They also appear to have a systematic dependence on latitude rather than an approximately constant value, producing a lower (~94 km) mean mesopause near ~5-25°S. This pattern is repeated in other subsets of the May-July data for local times around midnight, but not for times much earlier in the evening or later in the morning. Note, these mean altitudes were each determined from a single average temperature profile for events within a particular LT/latitude bin, not by averaging the individual events' mesopause altitudes. Therefore, the fact that the distributions shown in Figures 1 and 2 are also skewed to lower altitudes near ~5-25°S is a separate indication that some physical mechanism lowers the mesopause there; it is not a redundant confirmation of the pattern seen in the mean altitude.

Figure 3 gives a different, and perhaps more useful, view of the spread of mesopause altitudes. For 6-degree bins spaced throughout the range of latitudes, it shows the distribution for events near local midnight during the latter part of June and early July. The last six frames depict the high "regular" mesopause exclusively, and one can see a spread of ~5 km about the centroid in each case. In contrast, the first four frames show the low "summer" mesopause. At the most northerly latitudes, the distribution is very narrow, no more than ~2 km about the centroid, but it broadens as the latitude approaches the transition region.

It is particularly noteworthy that, in the summer high latitudes, the mesopause altitude shown in Figures 1 and 2 increases by about 5 km between 40°N and 82°N. This was hinted at in the *Polarstern* data and predicted by the aforementioned model study [*Berger and von Zahn, 1999*]. However, this is the first time that such a result has been confirmed at far northern latitudes, past 69°.

The polar summer mesopause altitudes shown here, and appearing in other subsets of SABER data, are consistently lower by ~2-3 km than is typically observed [*Lübken et al., 1999*]. This is easy to see because of the narrow distribution there, but from Figure 1— and more clearly from other SABER data—the regular mesopause also appears to be ~2-3 km below its nominal height of 100 km. As a result of this, the question of whether there is a bias in the SABER altitudes has been raised. A review of the pressure registration procedure, which could have induced an error of that magnitude, was conducted, but the changes that were instituted appeared to have a minimal effect. To verify this, we compared two days' data processed with the preliminary version 1.06 software with some of the older v1.04 data. The new results reflect a number of changes in addition to the pressure registration, but the new mesopause altitudes were within ~2 km of the old ones for almost all events. More importantly, there was no systematic difference; the distributions were practically unchanged. Therefore, the discrepancy between SABER mesopause altitudes and previous measurements, particularly in the summer polar region, remains a mystery.

In Figure 1, a small but not negligible number of events in the winter hemisphere have very low mesopause altitudes. In similar format, Figure 4 shows the altitude distribution in the afternoon (LT 15-16 h) using data taken during July. In this case, a much larger number of events south of the transition zone have this characteristic and, as a result, the transition zone itself is far less distinct. In contrast, during morning hours (7-9 LT; not shown) there are few very low-mesopause events. This apparent dependence on local time suggests a tidal influence. The tides are particularly strong in the upper mesosphere and they perturb the temperature profiles considerably. Part of our future effort will be to model these effects explicitly.

In order to investigate this, we looked at many individual events throughout the yaw cycle. We found a lot of events with what appears to be strong tidal or other wave structure superposed upon what one might suppose to be the mean state. (This is especially so in the winter hemisphere.) This raises the question of whether the definition of the mesopause as the super-stratopause temperature minimum is reasonable. Three retrieved temperature profiles shown in Figure 5 illustrate the problem. They come from three consecutive events in the southern hemisphere, from orbit 8492 on July 5. They each have two temperature inversions and three minima between the stratopause and the thermosphere. Despite their apparent similarity, we derive very different mesopause altitudes of 90, 67, and 103 km for them. For event 83 in particular, the one with the highest mesopause, the three widely-separated minima are less than one degree different in temperature, as indicated in Figure 5. Many other events have structure quite like these, and some of them produce the low-mesopause points that we find in the altitude plots.

The question still remains as to what produces large temperature inversions like those in Figure 5. Tidal amplitudes are not as large as the TILs shown here, but nonlinear wave-wave interactions involving the tides are thought to be capable of augmenting

4

them. Whatever the exact process is, it seems clear from these and many other SABER profiles that wave effects have a profound effect on the retrieved temperature and hence on the mesopause parameters derived from them. The existence of a very low-altitude mesopause is most likely due to such wave activity. This argues for a redefinition that requires averaging not only over short periods to eliminate gravity wave perturbations, but also over longer periods as well to eliminate the effect of tides [*Berger and von Zahn*, 1999]. Given the slow precession of the TIMED orbit, of course, the latter procedure would drastically compromise the SABER temporal resolution.

Figures 6 and 7 show the mesopause temperatures corresponding to the two sets of events depicted in Figures 1 and 2. The cold polar summer mesopause is apparent in each, as is a gradual (rather than abrupt) transition from "summer" to "regular" conditions. The full range of temperatures in the winter hemisphere is quite large, ~40 K. The temperature of the mean profiles varies by ~15 K over the latitude range 20°N-50°S for the July 5 data. The spread of temperatures north of the transition region is about half of what it is in the south.

Figures 8a-c, using nighttime data from 5 July, illustrate how the temperature structure changes through the transition region between the "summer" and "regular" regions. These figures show that the cold summer polar mesopause (Figure 8a) evolves into a double-minimum structure at northern mid- and low latitudes (Figure 8b) before transitioning to the high regular mesopause (Figure 8b-c). Wave structure is noticeable in some of the plots, despite the fact that each average is derived from 20 or more individual profiles from the full range of longitudes. This indicates that there is similar structure from event to event, and it is most likely driven by processes that are consistent from place to place—rather than sporadic in nature as, for example, gravity waves are.

Studying characteristics of the mesopause is an obvious and important application of the SABER database. The major advance that it represents is in its near-global coverage, and the sheer number of individual measurements it provides (~1400 events per day). For example, evidence for the existence of the global two-level mesopause has been pieced together from many past measurements made at various locales by different techniques and at different times. SABER now provides a single database capable of validating the notion. The results that we have examined from this one 60-day period certainly support the idea. They also show that, besides describing the mean state of the atmosphere at a given time and locale, we have an unprecedented view of the variability of the MLT region as well. One finds that the altitude of the mesopause is quite variable, more so in the winter hemisphere than in the summer, but the mean altitude is fairly stable. One finds an abrupt altitude transition from "summer" to "regular" conditions, but a smooth transition for the temperature. In fact, SABER data provide an ideal tool for studying the transition region, as suggested by Figure 8. There is a large range of mesopause temperatures at any given latitude in the winter hemisphere, but a much smaller range in the polar summer. Moreover, there are a lot of events displaying evidence of severe wave activity, which can cause the mesopause to appear at anomalously low altitudes.

We have also verified the prediction that the altitude of the low polar summer mesopause increases smoothly by ~5 km between 40 and 80°N.

5

The SABER data prove that a complete picture of mesopause characteristics requires more than a snapshot in time or space. Despite the rich and detailed information it provides, however, the difficulty of distinguishing between diurnal and seasonal changes remains. This problem arises because of the slow precession rate, which allows us to view most local times only once every yaw cycle, and the tides, which strongly modulate conditions of the MLT region on an hourly basis. We think that the best way to resolve these difficulties is to produce a detailed (and even redundant, using different years) view of data throughout the full parameter space (latitude/LT/season), and complement that with an effort to model tidal effects.

2.2. Mesospheric Temperature Inversion Layers

As noted above, the SABER database provides an unprecedented opportunity to study the global behavior of mesospheric temperature structure. One particularly interesting feature is the temperature inversion layer (TIL). Mesospheric TILs, which have been the subject of great research interest in recent years [e.g., *Leblanc and Hauchecorne, 1997; Meriwether and Gardner, 2000; Meriwether and Gerrard, 2004; Sassi et al., 2002; Huang et al., 1998; 2002*], appear with regularity in the SABER data. Each of the temperature profiles shown in Figure 5 in the preceding section has more than one TIL. As noted there, wave structure may perturb the mesosphere in many ways, even to such an extent that the mesopause appears at very low altitudes. We have come upon a number of events with TILs that are more than twice as large as the ones shown in Figure 5, having amplitudes as great as 100 K—the "amplitude" being defined as the temperature difference from an underlying minimum to a local maximum ~5-10 km higher up. This section describes an investigation of the TIL phenomenon as seen in the SABER data.

The first step we have taken is to determine when and where TILs are most likely to appear. That is, we wished to determine, for different seasons of the year, the latitudes, local times, and altitudes where they are seen and, conversely, where they are not seen. The discrimination according to LT is important because of the role of the tides, which is not completely understood [e.g., *Meriwether and Gerrard, 2004*] but clearly a factor in producing them.

This point is illustrated in Figure 9. In that figure, we juxtapose the mean temperature profiles at the equator for all events on the ascending and descending portions of the orbits for a single day in March 2002, and plot their difference as well. The local times for these events were approximately 0.1 h and 9 h, respectively. The profiles are offset by more than 50 K at two places, much more than the rms deviations that are also plotted. The mesopause altitudes and temperatures are distinctly different, and a TIL of more than 60 K amplitude appears on the ascending (nighttime) side. The difference plot reveals the tidal influence most strikingly. Oscillations with a vertical wavelength of ~22-25 km and an amplitude increasing with altitude point to the diurnal tide as the predominant influence—as expected at the equator at this time of year—despite the fact that the local times are less than 12 h apart. The size of the temperature differences is surprising, since the diurnal amplitude is expected to be only ~10-15 K in the upper mesosphere in March [*GSWM, 2004*].

Figures 10 and 11 depict several nighttime events with TILs. In Figure 10, events of March 27, 2002, include one extremely large TIL (event 4). One can see that the altitudes

6

at which these layers occur vary considerably. Many of the largest ones appear between ~83 and ~93 km (as shown in Figure 10), but the full altitude range extends at least 10 km above and below those points. We find that, when TILs appear in event after event, as on the two orbits chosen here, the variation of the altitudes is usually systematic rather than random. That is, the heights change gradually with latitude, and frequently repeat the pattern on consecutive orbits. Figure 11 shows four consecutive events with TILs all centered near ~80-84 km, from an orbit of July 13, 2002.

In order to examine TIL occurrence rates, we analyzed data from three complete yaw cycles in 2002 and 2003. Two cycles began near equinox, one looking north and one south, and one near solstice was north-looking. There were significant data drop-outs in each period, but we were still able to cover most of the latitude/LT parameter space, which we separated into 3-degree latitude bins and 1-hr LT bins. We determined the percentage of events with TILs larger than certain thresholds, and the mean altitude of such layers, for each bin and for each yaw cycle. The thresholds were 10, 20, and 40 K.

Probability results for the two equinox cycles are given in Figure 12 for 20-K TILs. It shows that inversion layers are strongly correlated with LT, and also that the variation with LT depends on latitude. There appear to be more TILs during the March-May period than during the September-November period, but in both cases we find a heavy concentration throughout most of the nighttime near the equator. We also find a somewhat lighter concentration in the early morning and a much lighter concentration in the early afternoon near 30 degrees in the spring hemisphere, plus some in the early morning near 30 degrees in the fall hemisphere. There are very few at latitudes polewards of 60 degrees.

One remarkable discovery is that TILs of this size appear with a likelihood exceeding 90% near the equator at certain times. Even for 40-K TILs (not shown), it approaches 50% in the late evening.

Figure 13 gives the mean TIL altitude for these two cycles, in the same format. For most of the bins, the distribution of altitudes has a single peak with a half-width (rms deviation) of only ~2 km. However, there are some regions of the parameter space where the distributions are either quite broad or bipolar, which makes the quantity less meaningful. Nevertheless, one sees that the altitudes definitely correlate with LT and latitude in much the same way as the probabilities do. At the equator, for example, the TILs tend to be just above 80 km at night (as shown in Figure 10) and much higher in the daytime (where they are also less numerous). At mid-latitudes, the average nighttime TIL is much higher, also in accord with Figure 10.

These two yaw cycles are consistent in that there is a fairly clear indication of diurnal patterns at the equator where the diurnal tide is strongest (especially near equinox), and a somewhat less clear indication of semidiurnal behavior near mid-latitudes where the semidiurnal tide tends to dominate. This can be seen in both the probabilities and the altitudes of the TILs. Note that the patterns north and south of the equator following the March equinox are similar to those south and north of it, respectively, following the September equinox.

For the solstice cycle that we examined, May-July 2003, there were numerous missing data. However, one can see from Figure 14 that the likelihood of finding TILs as large as 20 K is substantially less than near equinox for all regions of the parameter space. There

is still a small concentration at night at the equator, and also in early morning and late afternoon at midlatitudes in the winter hemisphere. The mean altitudes (not shown) of the TILs that are seen do vary with LT, but the data are too sparse to make much of the patterns. There are virtually no large TILs in the summer polar region, which seems consistent with the fact that the lapse rate is so large there.

Besides quantifying the distributions, a second task was to determine whether or not coherent inversion structures commonly persist over extended distances (hundreds or thousands of kilometers) in the horizontal direction. This is important for several reasons, among which are the fact that a large-scale TIL may comprise a stable duct for long-distance propagation of gravity waves, and/or support mesospheric undular bores [*Dewan and Picard, 1998; 2001*]. This may also shed some light on the role of gravity waves in producing TILs [*Huang et al., 1998; Liu et al., 2000*]. We therefore sought layers that were similar in amplitude and altitude within sequences of consecutive events. Our criterion was that qualifying events should all have TILs exceeding the chosen threshold (usually 20 K) at altitudes differing by no more than 3 km.

The along-track direction of motion is mainly north-south at latitudes where most TILs occur, and events are separated by 300-400 km. We find that sequences of six or more 20-K TILs, representing ~2000 km or more in distance, are very common, and we found several extending beyond 4000 km. Even with the more restrictive 40-K requirement, sequences of ~2000-3000 km are common near the equator. In general, the prevalence of extended TILs mirrors the probability that they occur at all, insofar as they are much less common or absent at high latitudes and solstice.

From this, one concludes that inversion layers very often do appear as extensive structures, at least in the north-south direction for some latitudes and times of day. One might assume that the same is true in all directions, but it is difficult to demonstrate this because consecutive orbits are separated by more than 2000 km (at low latitudes) and 90 minutes. Also, LT remains nearly unchanged. Therefore, even if similar structure were observed within a latitude region during consecutive events of two or more successive orbits, one could not tell whether it was static and long-lived or changing with the phase of the tide.

Understanding the role of the atmospheric tides in producing TILs is a third, and very important, reason for studying their global behavior. We have begun a modeling effort using the state-of-the-art Global Scale Wave Model [*GSWM, 2004*] to try to explain the SABER occurrence probabilities and amplitudes discussed earlier. Although this effort is far from complete, we have made some simple comparisons of TIL altitudes with GSWM predictions. In Figure 15, we plot centroids of TIL altitude distributions against local time for events near the equator during the March-May yaw cycle. We also plot the altitude of maxima in the tidal temperature perturbation from GSWM. The model altitudes descend regularly by about 25 km in 24 h, as expected for a dominant diurnal component. From ~4 h to 24 h LT, the TIL altitudes also descend, somewhat more gradually but in approximate agreement with the model. However, from ~0 h to 8 h, TIL altitudes between ~80 and 85 km do not vary with LT. (From 4 to 8 h, there is a bipolar distribution.)

This behavior appears to be consistent with conclusions drawn by Meriwether and Gerrard [*2004*]. They distinguish two types of mesospheric TILs: a "higher" TIL, in the altitude range ~85-100 km that is tidally driven and amplified by nonlinear gravity-wave

interactions; and a "lower" type, below ~80 km, that is caused by dissipating planetary waves. The "higher" TILs are typically characterized by a downward phase progression, which is similar to that shown in Figure 15. "Lower" TILs are normally not correlated in such a way, also in accord with the lower range shown here. It therefore seems possible that our observations can be explained in these terms, even though the lower range in Figure 15 is above 80 km. (According to Meriwether and Gerrard [*2004*], the complexity of the processes involved in TIL formation sometimes obscures the distinction between the two types. For example, variations in the strength of the tide on a particular day could modify the altitude range in question.) However, it is premature to draw broad conclusions from this one sample. In fact, we find that at 30°S, TIL altitudes above 85 km in the early morning—the only time at which they are numerous and the distribution is narrow—descend with LT at a rate much lower than that of the GSWM temperature maximum. To carry this further, it is important to refine the process whereby TIL altitudes are determined. It is also important to develop the model fully, utilizing complete temperature profiles for full latitudinal and seasonal ranges, in order to be definitive about the information that SABER yields about the relation between the migrating tides and TILs.

3. MODELING MESOSPHERIC BORES

3.1. Introduction

Bores are a class of waves that can propagate with large amplitudes over long distances in a channel. Their propagation characteristics have been studied both analytically and computationally using, for example, special solutions to the Navier-Stokes equations (NSEs). These nonlinear partial differential equations describe the momentum, continuity, and energy relationships that govern fluid flow in general, including the behavior of air parcels undergoing adiabatic motion in the case of atmospheric bores. The influences of gravity, temperature, and pressure on the fluid parcels are also incorporated into the NSEs. Although tropospheric bores have been observed, studied, and modeled, it has only been relatively recently that airglow emissions in the mesosphere have been imaged and associated with the passage of ducted bore fields [e.g., *Taylor et al., 1995; Dewan and Picard, 1998; Dewan and Picard, 2001; Smith et al., 2003; She et al., 2004*]. The ducting regions in these cases are understood to be formed by a strongly stable layer, above and below which are weakly or neutrally stable regions. Such guiding structures can be caused by temperature inversion layers and certain types of wind profiles.

Although there have been investigations of bores in other contexts using assumed analytical models for both the background wind profile $U_0(z)$ and the Brunt frequency $N(z)$, we were interested in using actual mesospheric *measurements* of key physical variables such as temperature and wind. N in this report is the natural buoyancy frequency at which air parcels oscillate parallel to a vertically directed gravitational field and is determined by the temperature and the lapse rate. The data used in this report were lidar measurements [*She et al., 2004*] of temperature and background wind profiles for a bore field being ducted in the mesosphere and also included the observed bore speed from a CCD imager. The data and the bore speed observed by these authors provide a basis against which predictions from a mathematical model can be compared. Our first objective was thus to develop a space-time evolving, ducted mesosphere bore field model

and to compare the predictions from it with their observations. Having such a model, one could then use its evolving displacement amplitude to quantitatively estimate the strength of airglow emissions at any altitude in the mesosphere.

One approach for creating the desired mathematical model is to pose and solve an initial-value boundary-value problem involving the fluid dynamical NSEs, since they define the physics governing the motion of air parcels. Following Ono [*1975*], we used a weakly nonlinear analysis and obtained a separation of variables solution to the NSEs. This led to a description of vertical air parcel displacements $\varsigma(x, z, t)$ caused by the passing bore, in which $\varsigma(x, z, t)$ is found to be proportional to the product of the functions $\phi(z)$ and $A(x, t)$. $\phi(z)$ satisfies the Taylor-Goldstein (TG) equation and $A(x, t)$ emerges from the solution to the Benjamin-Davis-Ono-Burgers (BDOB) equation. More will be said about both equations shortly.

Ono's analysis did not meet our needs entirely; it lacked the effect of a background wind profile, and his derivation was based on the assumption of a purely *in*compressible fluid. The effect of compressibility was needed for our model since the mesosphere fluid is composed of air parcels. Compressibility was eventually incorporated into our analysis using an approach taken by Doviak et al. [*1991*] and Christie [*1989*] whereby temperature and density are replaced by potential temperature and potential density, respectively. This will also be discussed shortly.

3.2. Formulation of Taylor-Goldstein and Helmholtz Equations

Pursuing an Ono type of derivation for an incompressible fluid [*Ono, 1975*], but now including an arbitrary background wind profile, two basic equations emerge: the TG and BDO equations. The latter is the same as the BDOB equation but without the Burgers loss term added in. Compressibility influences will be accounted for in another way.

The TG equation [*Doviak et al., 1991; Christie, 1989*] eigenmodes are assumed to be governed in the long-horizontal-wavelength limit by

$$(\rho_0 \phi')' + \phi \left\{ \frac{N^2 \rho_0}{\left(U_0(z) - c_0\right)^2} - \frac{\left(\rho_0 U_0'\right)'}{\left(U_0(z) - c_0\right)} \right\} = 0, \qquad -\infty \leq z < \infty. \tag{1}$$

(Primes indicate differentiation with respect to z in this report.) $\phi(z)$ is the long wave eigenfunction and c_0 is the eigenvalue phase speed associated with the bore. Both are to be determined. Homogeneous boundary conditions of the form $\mu \phi' + \phi = 0$ at $z = -\infty$ and at $z = \infty$ are imposed for the solution of Equation 1. In practice, we find that there is no significant difference in the value of c_0 for the lowest modes, relative to other effects and approximations inherent in our formulation, whether one uses Dirichlet, Neumann, or mixed boundary conditions.

For reasons discussed in the next section, the TG equation is transformed to a Helmholtz equation using the exponential stratification factor contained in

$$\phi = W \exp\left(\frac{1}{2} \int_z dz' / H(z') \right) \quad \text{with} \quad H = -\frac{\rho_0}{\rho_0'}. \tag{2}$$

Substituting into the TG equation, one arrives at the Helmholtz equation $W'' + k_z^2 W = 0,$ with the propagation constant $k_z(z)$ given by

$$k_z^2 = \frac{N^2}{\left(U_0(z) - c_0\right)^2} - \frac{\left(\rho_0 U_0'(z)\right)' / \rho_0}{\left(U_0(z) - c_0\right)} - \frac{1 + 2H'}{4H^2}. \tag{3}$$

In this equation and following the lead of Doviak et al. [*1991*], the presence of N^2 indicates that compressibility was accounted for by relating density (ρ_0), potential temperature (θ), and Brunt-Vaisala frequency squared (N^2), respectively, as follows:

$$\frac{\rho_0'}{\rho_0} \rightarrow -\frac{\theta'}{\theta} = -\frac{N^2}{g}, \quad \text{with} \quad \rho_0 \rightarrow (const)\theta^{-1}(z);$$

namely, the logarithmic derivative of the density was replaced by the potential temperature and its derivative. Figure 16 shows the resulting k_z^2 in the data window for the case of 3-point smoothing of $U_0(z)$. Several positive regions indicate the presence of *multiple* mesosphere ducts that allow for propagating modes to be supported.

The wind profile $U_0(z)$ used in Figure 16 and the calculations discussed herein are from the work of She *et al.* [*2004*]. The data were originally sampled at 0.5 km altitude increments, subsequently smoothed, and then spline interpolated.

3.3. Altitude-Limited Data Considerations

Several complicating factors arose in the modeling effort associated with the altitude-limited data from the lidar. The formulation for the mathematical model requires that all terms in the TG equation be specified for the entire altitude range spanning $(0, \infty)$ or, to an excellent approximation, $(-\infty, \infty)$. However, ground-based sodium lidar measurements of the event [*She et al., 2004*] are available only over a *finite* altitude range, ~83-100 km. Under these conditions, one can only hope to approximate the properties of the evolving bore field. This necessitated making assumptions about field behavior and medium properties *outside* the lidar data measurement window.

Another difficulty is that the altitude-limited measurements of temperature $T(z)$ and background wind profile, $U_0(z)$, contain noise. Both of those functions, as they appear in the TG equation, need to be differentiated numerically to yield $N^2, U_0',$ and U_0''. Despite initially smoothing both T and U_0, data differentiation of any residual spatial variations in these functions after smoothing was found to affect the value of the phase speed eigenvalue, significantly so in some cases we studied. The "best" way to smooth and differentiate the data in the context of solving the TG equation has not been extensively examined to the best of our knowledge. We experimented with various

smoothing techniques applied to the data of She et al. [2004], and settled on a simple triangle weighting that averaged the central point with its 2, 4 or 6 nearest neighbor points.

Without any information about the background wind at altitudes above and below the data window at the time of the event, we made a simplifying assumption consistent with some earlier studies; namely, that U_0 is taken to be spatially uniform, though not necessarily of the same value above the data window as below. Each of these two values is pegged to the wind speed just inside the nearest border of the data window. The spatial uniformity of U_0 implies that above and below the window, U_0' and U_0'' vanish. The assumption of spatial uniformity of U_0 is not, however, absolutely required [Doviak et al., 1991]. The situation described therein seemed too exceptional and unlikely to be of interest to us; specifically, it implies a functional relationship between potential temperature and the background wind profile.

Yet another consequence of having altitude-limited data is the matter of how to specify TG equation terms that govern mode shape outside the data window. We approached this issue by first noting that ducted wave propagation in general is more easily examined using the Helmholtz equation, $W'' + k_z^2(z)W = 0$ when possible. We thus transformed the TG equation to the Helmholtz equation using the standard exponential stratification factor (see Equation 2) and solved for eigenmodes of the Helmholtz equation. Once the solutions were obtained, the resulting field was transformed back to the TG field variable $\phi(z)$. Following this approach, we dealt with the problem of a finite data window by approximating the Helmholtz mode outside the data region with two decaying exponentials, one on each side of the window. These exponentials were connected to the solution inside the data window at the borders and made to vanish asymptotically for $z \to \pm\infty$. Outside the window, terms in k_z^2 (see Equation 3) composed of $N^2, U_0', \text{and} U_0''$ vanish, leaving the small negative factor, $-\nu^2 = -(1 + 2H')/4H^2$, which if *spatially averaged* defines a decay constant in each of the two regions outside the window. Here, H is an altitude-dependent pressure scale-height, the values of which were not available outside of the data window at the time of the bore event but were obtained, expediently, from an available (ALOHA) atmosphere model and some piece-wise temperature fittings using formulas from the U.S. Standard Atmosphere. While this would appear to yield a gross approximation at any particular altitude at the time of the event, as an averaged quantity, using this type of approximation led to phase speed results not too far from the observed bore speed, namely, within 10%. This rationale is also in keeping with our understanding from other work and observations that the local state of the atmosphere away from the mesosphere data window has a relatively minor influence on bore characteristics. In future endeavors, however, we would recommend a more judicious choice of model atmosphere from which to develop H. The values assigned to the exponential decay constants in this investigation were thus obtained by spatially averaging $-\nu^2$ for each of the two regions outside the data window.

3.4. Solution of Taylor-Goldstein and Helmholtz Equations

Both from physical considerations and because the data used was space-limited, we sought a solution method emphasizing data in the window and de-emphasizing or requiring less information about conditions outside of it. To this end, we developed a solution representing the lowest-order bore modes using rational Chebyshev polynomials $TB_m(z)$ [Boyd, 2000] by letting

$$W(z) = \sum_{m=0}^{2M} C_m \cdot TB_m(z). \qquad -\infty < z < \infty \qquad (4)$$

Applying the following cotangent-mapping, with θ now denoting angle, not potential temperature,

$$z = -L\cot(\theta) + \overline{z} \ , \text{ with } 0 \leq \theta \leq \pi, \qquad (5)$$

and using a Gauss-Lobatto [Boyd, 2000, p.570] discretization over the angle via $\theta \rightarrow \theta_l = l\pi/2M$ $(l = 0,1,...,2M)$, one finds that the density of altitude samples is greatest about the mid-altitude $\overline{z}$ of the data window $[a,b] = [83,100]$ km (see Figure 17). We note that for $M = 70$, 92% of the nodes fall within the data window, while for M = 100, the number is 94%. The $\cot\theta$-mapping in this context also allows one to use the equivalent but more easily manipulated expansions,

$$W_M(\theta) = \sum_{m=0}^{2M} C_m \cos m\theta \quad \Rightarrow \quad W_{M,l} = \sum_{m=0}^{2M} C_m \cos m\theta_l . \qquad (6)$$

The tuning parameter L can be chosen in various ways. For this investigation, L was adjusted so that $L = \dfrac{\overline{z}}{\cot(0.5\pi/2M)}$ with the 1st node being set at $z = -10^8 km \approx -\infty$ where we set W = 0.

At altitudes outside the data window, the Helmholtz eigenmodes were approximated by using spatial averages of $\nu^2 = (1 + 2H')/4H^2$, now equal to a constant below the window and to another constant above the window, as discussed in the previous section. This created decaying exponential Helmholtz mode shapes outside the data window.

Substituting Equation 6 into the Helmholtz equation, after observing that

$$\frac{d}{dz} = \frac{d\theta}{dz}\frac{d}{d\theta} \quad \text{and} \quad \frac{d^2}{dz^2} = \frac{1}{L}\frac{d\theta}{dz}\left(\sin 2\theta \frac{d}{d\theta} + \sin^2\theta \frac{d^2}{d\theta^2} \right) \qquad (7)$$

yields the following linear, homogeneous system of equations:

$$-\frac{\sin^2\theta_l}{2L^2} \sum_{m=0}^{2M} C_m \left\{ \begin{array}{l} m[\cos(m-2)\theta_l - \cos(m+2)\theta_l] + m^2\cos m\theta_l \\ -\dfrac{m^2}{2}[\cos(m+2)\theta + \cos(m-2)\theta_l] \end{array} \right\}$$

$$(8)$$

$$+k_z^2(\theta_l; c_0) \sum_{m=0}^{2M} C_m \cos m\theta_l = 0 \qquad \text{for } l = 0,1,...,2M.$$

The method used to determine a specific mode is described next.

The determinant of the system was evaluated numerically for any specified trial value of c_0. Stepping through a sequence of trial values, and calculating the corresponding determinant for each resulting set of equations, the c_0 interval in which a root (eigenvalue) was located could be identified by a sign change in consecutive determinant evaluations. A root-finder was then used to converge to the final phase speed eigenvalue. Having obtained c_0, the expansion coefficients were determined in the standard way by normalizing the coefficients, dropping one equation, and solving the resulting inhomogeneous system. By repeating this solution method several times with successively increasing values of *M*, a 2-pass application of Aiken's convergence acceleration method [*Press et al., 1986*] on the rational Chebyshev polynomial partial sums yields phase speed estimates of 67-68 m/s. Figure 17 shows an example of the Helmholtz eigenmode thus obtained. The convergence of the predicted phase speed versus *M* is shown in Figure 18. Also shown in Figure 18 is the result of a curve fitting experiment using *tanh* functions to express $c_0(M)$ at successively increasing values of *M*. Extrapolating $M \to \infty$ yields the phase speed estimate indicated in Figure 18, and tends to the same value that the Aiken's extrapolation produced.

Based on observations and measurements by She et al. [*2004*], we were especially interested in bores traveling at or near 74 m/sec. We bracketed our search for a mode traveling between 60-120 m/sec. This led to the 2nd lowest-order varicose-like mode. Multiple eigenvalues corresponding to higher-order modes with slower phase speeds were also detected when we applied the same algorithm to lower speed ranges. In addition, there was a heretofore unobserved lowest-order mode that appeared at ~168 m/sec.

Having obtained the Helmholtz mode of interest and the associated phase speed estimate, the corresponding TG mode is obtained using Equation 2. Here, however, we must account in some manner for losses due to the effects of molecular viscosity, eddy dissipation, and thermal conduction above the data window. We used a small, short range loss factor that varies parabolically with altitude from and above the top of the data window for this purpose. Qualitatively, the resulting $\phi(z)$ appearance now makes more sense physically than it does without the loss function.

In summary, we developed a new solution method for the Helmholtz and TG equation that addressed some of the issues associated with altitude-limited data resulting from lidar mesosphere measurements. Using data from She et al. [*2004*], the phase speed estimate we obtained with different wind profile smoothing was in the range of 67-68 m/s when one executes two passes of Aiken's convergence acceleration scheme on the partial sum expansion for the eigenmode shown in Equation 6. This procedure yields phase speed estimates within 10% of the observed bore speed, which was ~74 m/s. The mode shape bears a resemblance to varicose modes observed in other bore contexts.

3.5. The Benjamin-Davis-Ono-Burgers (BDOB) Equation and its Solution

The BDO equation governs the horizontally evolving dimension*less* stream function amplitude quantity $A(x,t)$ necessary to describe the bore displacement. When loss due to

eddy diffusivity is taken into account, an added (Burgers) term appears, leaving the BDOB equation in dimensionless form as

$$\frac{\partial A}{\partial T} + A\frac{\partial A}{\partial X} + \frac{\partial^2}{\partial X^2}H(A) - \varepsilon\frac{\partial^2 A}{\partial X^2} = 0,\tag{9}$$

where $H(A)$ is the Hilbert transform of A, $\varepsilon = \mu/\beta$, μ is the eddy diffusivity coefficient, and β is defined below.

To solve this nonlinear partial integro-differential equation, we embedded a pseudo-spectral method for the spatial variation of A into a Crank-Nicholson implicit time-stepping scheme [Carnahan et al., 1969]. Our choice for the particular algorithm used for the pseudospectral stage was one developed by James and Weideman [1992]. It is based on a Fourier series/domain truncation methodology. The truncated domain spanned a segment of the duct axis taken to be parallel to the earth's surface. The Fourier series were efficiently evaluated using FFT operations.

The dimension*less* variables (A, X, T) can be related to dimension*al* variables $(\tilde{A}, \tilde{\xi} = x - c_0 t, t)$ as follows:

$$A = \alpha(b-a)\tilde{A}/\beta,$$

$$X = \tilde{\xi}/(b-a), \text{ and}\tag{10}$$

$$T = \beta t/(b-a)^2.$$

$(b-a)$ is usually taken as the duct width. For several adjacent ducts, as shown in Figure 16, the definition of "duct width" becomes somewhat obscure. For the data window altitude range [83,100] km, we used a value of 17 km. We note that $\tilde{\xi} = x - c_0 t$ is the position variable in the Rayleigh frame moving at the phase speed c_0 with respect to the laboratory frame.

In the above formulas, the parameters α and β arise in the derivation for the BDOB equation and are given by the following formulas: $\alpha = \alpha_2/\alpha_1$ and $\beta = \alpha_3/\alpha_1$, where

$$\alpha_1 = \int\limits_a^b dz\, \frac{\phi(z)}{U_0 - c_0}\left\{(\rho_0\phi')' + \frac{g\rho_0'\phi}{(U_0 - c_0)^2}\right\},\tag{11}$$

$$\alpha_2 = \int\limits_a^b dz\, \frac{\phi(z)}{U_0 - c_0}\cdot$$

$$\left\{\left[\rho_0'\phi\phi' - \frac{\rho_0'U_0'\phi^2}{U_0 - c_0} + \rho_0(\phi'^2 - \phi\phi'')\right]' + \frac{g}{U_0 - c_0}\left[\frac{\rho_0'\phi'\phi}{U_0 - c_0} - \phi\left(\frac{\rho_0'\phi}{U_0 - c_0}\right)'\right]\right\},\tag{12}$$

15

and

$$\alpha_3 = \rho_0(b)\phi^2(b) + \rho_0(a)\phi^2(a).$$ (13)

The BDOB equation thus makes use of the previously calculated eigen-pair $\{\phi(z); c_0\}$ through the α, β parameters. Although the above formulas do not appear to resemble the ones obtained by Doviak et al. [1991], we are able to show that Equations 11 and 12 agree exactly with their results for an arbitrary wind when the Scorer approximation is invoked.

It is useful to integrate by parts some of the integrands shown in Equations 11 and 12. This allows one to a) minimize the presence of noisy higher-order derivatives in the numerical evaluation of the integrals and b) to take into account, in an approximate manner, compressibility effects as done by Doviak et al. [1991] using $g\rho_0'/\rho_0 \rightarrow -N^2$. After integrating by parts, one is left with boundary terms and integrals. Outside the duct and at the boundaries, those multiplied by $N^2, U_0', $ or U_0'' must be set to zero in keeping with the modeling assumption of a uniform wind below and above the duct as well as the vanishing of N^2 outside the duct. When this is done, we verified that the vertical and horizontal parcel displacements, as the bore passes any given point in its path, are qualitatively and quantitatively reasonable.

Figures 19-24 illustrate $A(X,T)$ as observed in the Rayleigh frame for several bores having different initial pulse amplitudes. For a small initial amplitude, e.g., $A(X,0) = 0.1$, as seen from Figures 21 and 22, the bore is predicted to travel *slower* than the long wave phase speed, at least over the time T-interval considered. This is manifested by the main peak moving backwards as T increases. For larger values of T, the bore speeds up and eventually travels faster than the long wave phase speed. The situation for larger amplitudes shows that the bore travels faster than the phase speed, at least for $T > 5$ (see Figures 19 and 20). We note also that the shapes of $A(X,T)$ generated in two examples using the BDOB code was verified by two published figures from Christie [1989].

The results for a very long pulse (shown in Figure 23) illustrate both the front steepening due to the nonlinearity and the rear flattening caused by dispersion effect arising from the Hilbert transform term. These effects are also apparent from the Figure 24 snapshot, where one can observe the trailing amplitude going negative.

Summarizing, we have obtained solutions to the BDOB equation using pseudo-spectral and Crank-Nicholson methods, the results of which have been confirmed with previously published figures found in Christie [1989]. We find that for a small initial amplitude pulse, the main peak of the bore travels *slower*, at least initially, than the long wave phase speed which corresponds to the speed of the Rayleigh frame. To the best of our knowledge, this effect has not been previously reported. As the pulse amplitude is increased, the bore moves faster. We have also examined situations involving short and long pulses, as shown in the figures. Steepening of the front and flattening of the rear of the evolving field are plainly visible as one expects from a bore analysis involving the nonlinear and Hilbert transform terms, respectively. A perhaps even more realistic analysis would replace the initial pulse, which appears instantaneously at time $T = 0$ in this

investigation, with one due to a source that develops over time. This remains to be investigated and would provide an even more realistic model of the evolving field. Having obtained both $\phi(z)$ and $A(x,t)$, the vertical parcel displacements can now be evaluated.

3.6. Vertical Parcel Displacements

Following the approaches of Ono [*1975*] and Doviak et al. [*1991*], using a stream function formulation, one can show that the vertical parcel displacements are given by the simple formula

$$\varsigma(x,z,t) = \left| \frac{\beta}{\alpha c_0 (b-a)} \right| \phi A \, , \tag{14}$$

in the limit of no loss ($\varepsilon = 0$). Figures 25-28 show examples of the evolving vertical displacement for an arbitrarily chosen fixed point x in the laboratory frame 500 km from the front of an initial pulse of length $\Delta X = 20$ or $\Delta x = (b-a)\Delta X = 340$ km.

Two types of figures are shown for the displacements; one is based on α and β containing only Scorer approximation terms, and the other also includes non-Scorer approximation terms. In the Scorer approximation, one uses in the derivation leading to $\varsigma(x,z,t)$, an approximation to the TG and Helmholtz equations; namely,

$$\phi'' + \phi \left\{ \frac{N^2}{(U_0 - c_0)^2} - \frac{U_0''}{U_0 - c_0} \right\} \approx 0. \tag{15}$$

Non-Scorer terms arise when one includes all of the terms in the TG or Helmholtz equation. From our study we find that there is a significant difference in the predicted maximum vertical displacements, which occur at an altitude of 100 km, when using the two parameter sets, as can be seen from Figures 25-28.

3.7. Summary of Results

To obtain the displacements, our analysis and the ensuing codes were based on a deep fluid model using altitude-limited measurements of temperature and background wind profiles. An initial-value boundary-value problem was posed and solved for this purpose. A separation of variables solution emerged from a weakly nonlinear formulation following the methodology of earlier investigators. Our investigation differs from earlier work by including the effect of a background wind profile based on lidar data measurements in the mesosphere. The separation of variables approach required us to solve the TG equation via a Helmholtz equation solution for the mode shape and long wave phase speed associated with the passing bore, which was ultimately necessary for parcel displacement calculations. A rational Chebyshev polynomial method was developed for the Helmholtz equation because of its emphasis on altitude data samples within the mesosphere data window. A rationale for treating the region outside the data window was also developed. The predicted phase speed was found to be within 10% of the observed bore speed. We then chose a pseudospectral/Crank-Nicholson solution method for solving the BDOB equation, this being the other equation emerging from the separation of variables solution. The computed horizontally varying component of the bore field agreed

with published figures for test cases. Based on our displacement calculations, we find that the Scorer approximation might be too restrictive to assume, especially if there are multiple ducts, as there appeared to be in the data we used. Pursuing a direct numerical simulation in a future effort would resolve this uncertainty. We also think it would be of considerable value to treat the source(s) of the bore more realistically by using a temperature or pressure time-varying source function rather than the impulsive source used in this study. Having developed programs for calculating evolving vertical parcel displacements at any altitude in the mesosphere, we are now in a position to use the displacements for quantifying airglow emissions.

REFERENCES

Berger, U., and U. von Zahn, "The two-level structure of the mesopause: A model study", *J. Geophys. Res.*, **104**, 22083-22093, 1999.

Boyd, J.P., Chebyshev and Fourier Spectral Methods, Dover Publications, 2nd ed, 2000.

Carnahan, B., Luther, H.A., and Wilkes, J.O., Applied Numerical Methods, John Wiley & Sons, New York, 1969.

Christie, D.R., "Long nonlinear waves in the lower atmosphere", *J. Atmos. Sci.*, **46**, 1462-1491, 1989.

Dewan, E.M. and R.H. Picard, "Mesospheric bores", *J. Geophys. Res.*, **103**, 6295-6305, 1998.

Dewan, E.M. and R.H. Picard, "On the origin of mesospheric bores", *J. Geophys. Res.*, **106**, 2921-2927, 2001.

Doviak, R.J., S.S. Chen, and D.R. Christie, "Thunderstorm-generated solitary wave observation compared with theory for nonlinear waves in a sheared atmosphere", *J. Atmos. Sci.*, **48**, 87-111, 1991.

GSWM: Global Scale Wave Model, web.hao.ucar.edu/public/research/tiso/gswm/gswm.html, 2004.

Huang, T.Y., H. Hur, T.F. Tuan, X. Li, E.M. Dewan and R.H. Picard, "Sudden narrow temperature-inversion-layer formation in ALOHA-93 as a critical-layer-interaction phenomenon", *J. Geophys. Res.*, **103**, 6323-6332, 1998.

Huang, T.Y., M.P. Hickey, T.F. Tuan, E.M. Dewan, and R.H. Picard, "Further investigations of a mesospheric inversion layer observed in the ALOHA-93 campaign", *J. Geophys. Res.*, **107**(D19), 4408, doi:10.1029/2001JD001186, 2002.

James, R.L., and J.A.C. Weideman, "Pseudospectral methods for the Benjamin-Ono Equation," in Advances in Computer Methods for Partial Differential Equations VII, IMACS, pp. 371-377, 1992.

Leblanc, T. and A. Hauchecorne, "Recent observations of mesospheric temperature inversions", *J. Geophys. Res.*, **102**, 19471-19482, 1997.

Liu, H.-L., M.E. Hagan, and R.G. Roble, "Local mean state changes due to gravity wave breaking modulated by the diurnal tide", *J. Geophys. Res.*, **105**, 12381-12396, 2000.

Lübken, F.-J, "Thermal structure of the Arctic summer mesosphere," *J. Geophys. Res.*, **104**, 9135– 9149, 1999.

Meriwether, J.W. and C.S. Gardner, "A review of the mesosphere inversion layer phenomenon", *J. Geophys. Res.*, **105**, 12405-12416, 2000.

Meriwether, J.W., and A.J. Gerrard, "Mesosphere inversion layers and stratosphere temperature enhancements", *Rev. Geophys.*, **42**(3), 8755, 1209/04/2003RG000133, 2004.

Mertens, C.J., M.G. Mlynczak, M. Lopez-Puertas, P.P Wintersteiner, R.H. Picard, J.R. Winick, L.L. Gordley, and J.M. Russell III, "Retrieval of mesospheric and lower thermo-

spheric kinetic temperature from measurements of CO_2 15 μm Earth limb emission under non-LTE conditions", *Geophys. Res. Lett.*, **28**, 1391-1394, 2001.

Mertens, C.J., M.G. Mlynczak, M. Lopez-Puertas, P.P Wintersteiner, R.H. Picard, J.R. Winick, L.L. Gordley, and J.M. Russell III, "Retrieval of kinetic temperature and carbon dioxide abundance from non-local thermodynamic equilibrium limb emission measurements made by the SABER experiment on the TIMED satellite", *Proc SPIE*, **4882**, 162-171, 2002.

Mertens, C.J., F.J. Schmidlin, R.A. Goldberg, E.E. Remsberg, W.D. Pesnell, J.M. Russell III, M.G. Mlynczak, M. Lopez-Puertas, P.P. Wintersteiner, R.H. Picard, J.R. Winick, and L.L. Gordley, "SABER observations of mesospheric temperatures and comparisons with falling sphere measurements taken during the 2002 summer MaCWAVE campaign", *Geophys. Res. Lett.*, **31**, L03105, doi:10.1029/2003GL018605, 2004.

Ono, H., "Algebraic solitary waves in stratified fluids," *J. Phys. Soc. Jap.*, **39**, 1082-1091, 1975.

Picard, R.H., P.P. Wintersteiner, J.R. Winick, C.J. Mertens, M.G. Mlynczak, J.M. Russell III, L.L. Gordley, W.E. Ward, C.Y. She, and R.R. O'Neil, "Tidal and layer structure in the mesosphere and lower thermosphere from TIMED/SABER CO_2 15 μm emission, *Proc. SPIE*, **5571**, in press, 2005.

Press, W.H., B.P. Flannery, S.A. Teukolsky, and W.T. Vetterling, Numerical Recipes: The Art of Scientific Computing, Cambridge University Press, London, pp. 132-133, 1986.

Russell, J.M. III, M.G. Mlynczak, L.L Gordley, J. Tansock, and R. Esplin, "An overview of the SABER experiment and preliminary calibration results", *Proc. SPIE*, **3756**, 277-288, 1999.

Sassi, F., R.R. Garcia, B.A. Boville, and H. Liu, "On temperature inversions and the mesospheric surf zone", *J. Geophys. Res.*, **107**(D19), 4380, doi:10.1029/2001JD001525, 2002.

She, C.-Y., T. Li, B.P. Williams, T. Yuan, and R.H. Picard, "Concurrent OH imager and sodium temperature/wind lidar observation of a mesopause region undular bore event over Fort Collins/Platteville, Colorado," *J. Geophys. Res*, **109**, D22107, doi:10.1029/ 2004JD004742, 2004.

Smith, S.M., M.J. Taylor, G.R. Swenson, C.Y. She, W. Hocking, J. Baumgardner, and M. Mendillo, "A multidiagnostic investigation of the mesospheric bore phenomenon", *J. Geophys. Res.*, **108**(A2), 1083, doi:10.1029/2002JA009500, 2003.

Taylor, M.J., D.N. Turnbull, and R.P. Lowe, "Spectrometric and imaging measurements of a spectacular gravity wave event observed during the ALOHA-93 campaign", *Geophys. Res. Lett.*, **22**, 2849-2852, 1995.

Thulasiraman, S. and J.B. Nee, "Further evidence of a two-level mesopause and its variation from UARS high-resolution Doppler imager temperature data", *J. Geophys. Res.*, **107**(D18), 4355, doi:10.1029/2000JD000118, 2002.

von Zahn, U., J. Hoffner, V. Eska, and M. Alpers, "The mesopause altitude: Only two distinctive levels worldwide?", *Geophys. Res. Lett.*, **23**, 3231-3234, 1996.

Winick, J.R., P.P. Wintersteiner, R.H. Picard, C.J. Mertens, M.G. Mlynczak, M.E. Hagan, W.E. Ward, J.M. Russell, and L.L. Gordley, "Global occurrence statistics of mesospheric inversion layers obtained from SABER temperature profiles," *Eos Trans. AGU*, **85**(46), Fall Meet. Suppl., Paper SA34A-06, 2004.
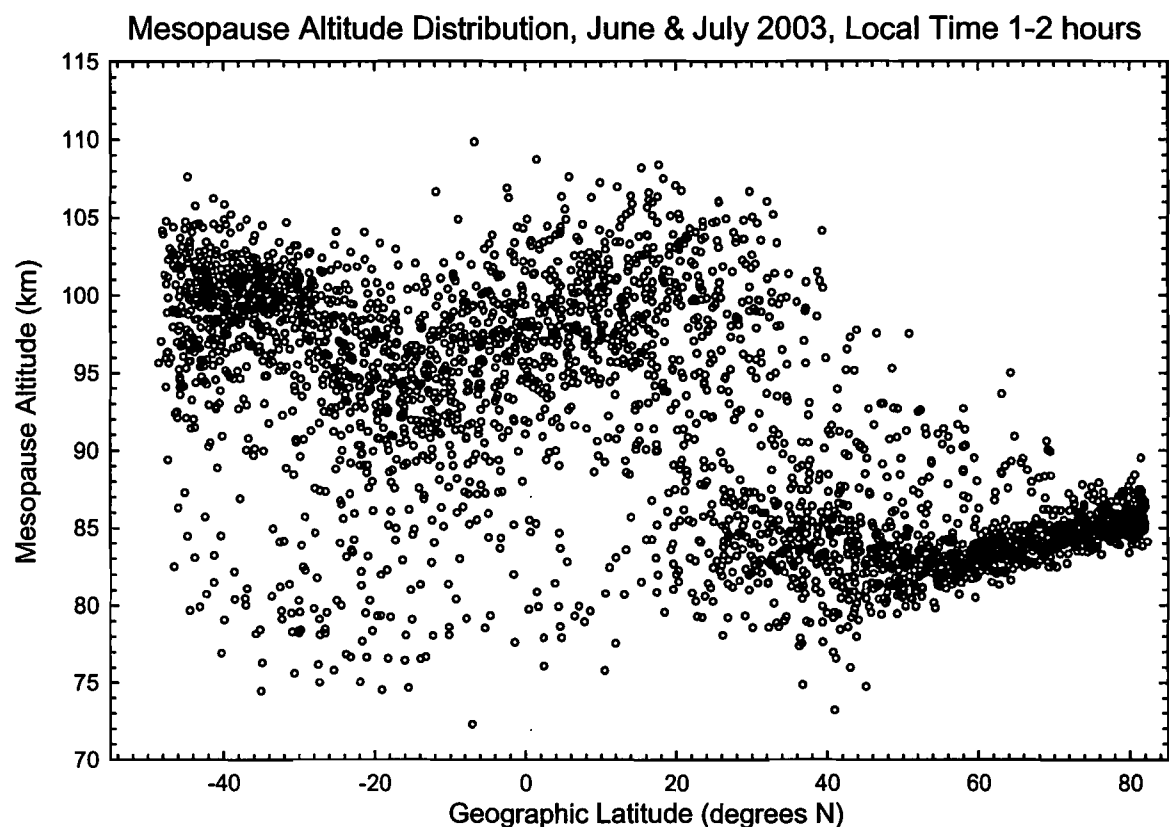
Figure 1. SABER mesopause altitude distribution as a function of latitude for 21 June-9 July 2003. All data are for local time 1-2 h.
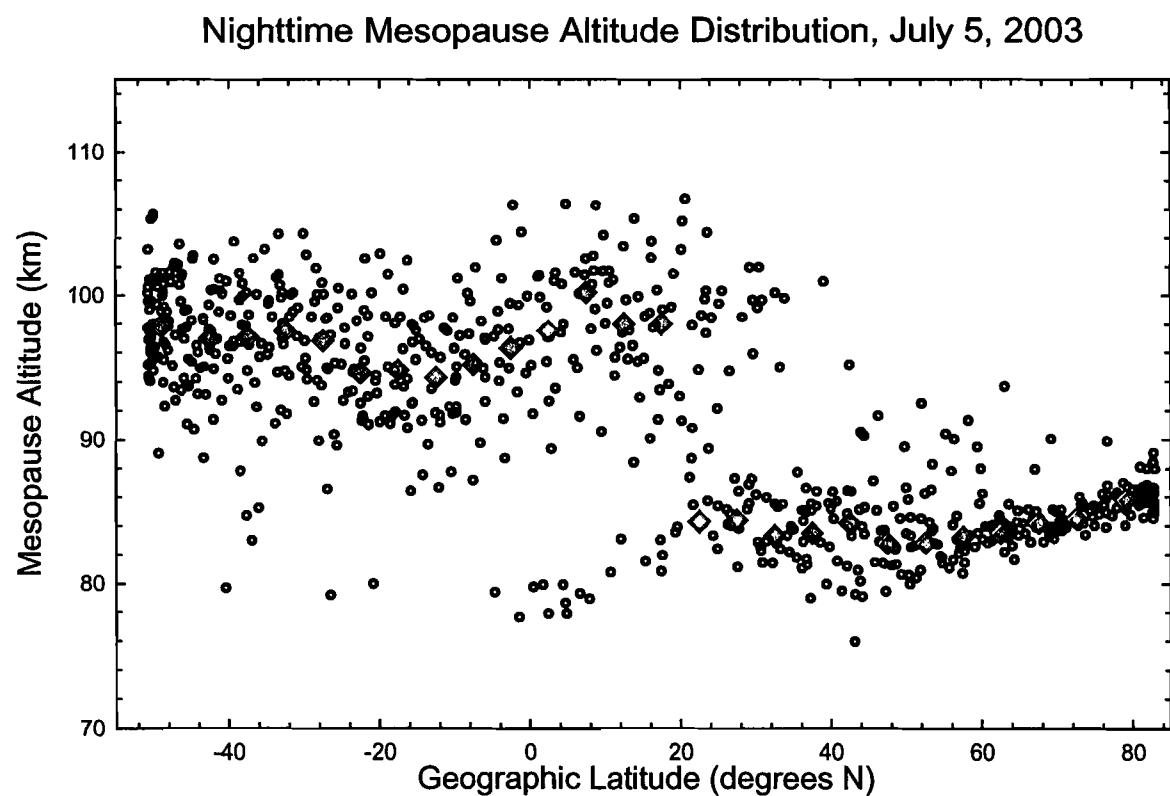
Figure 2. Similar to Figure 1, but using all ascending data from 5 July 2003 only. Local times were all between 20 h and 2 h. Mesopause altitudes calculated from mean profiles for 5-degree latitude bins are shown in red.

Figure 3. Distribution of nighttime mesopause altitudes, by latitude, in late June and early July 2003

Mesopause Altitude Distribution, July 2003, Local Time 15-16 hours
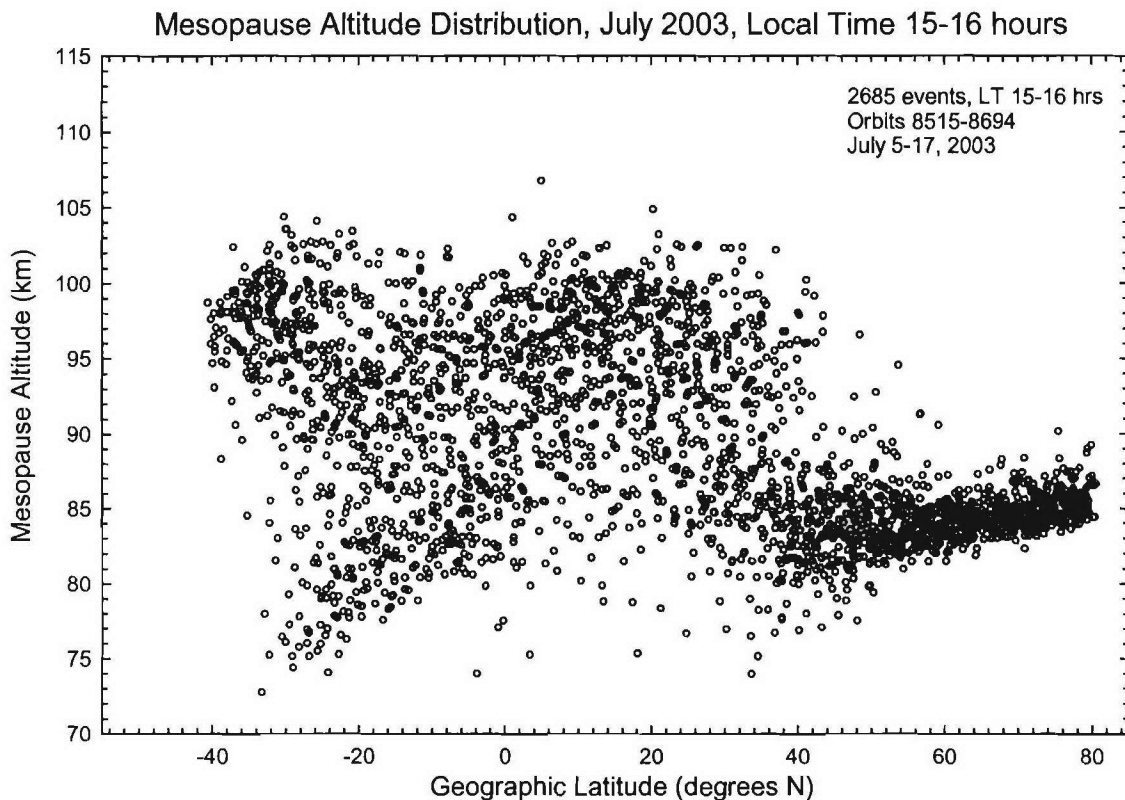
Figure 4. SABER mesopause altitude distribution as a function of latitude for 5-17 July 2003. All data are for local times 15-16 h.

July 3, 2003, Orbit 8492, Kinetic Temperature Profiles
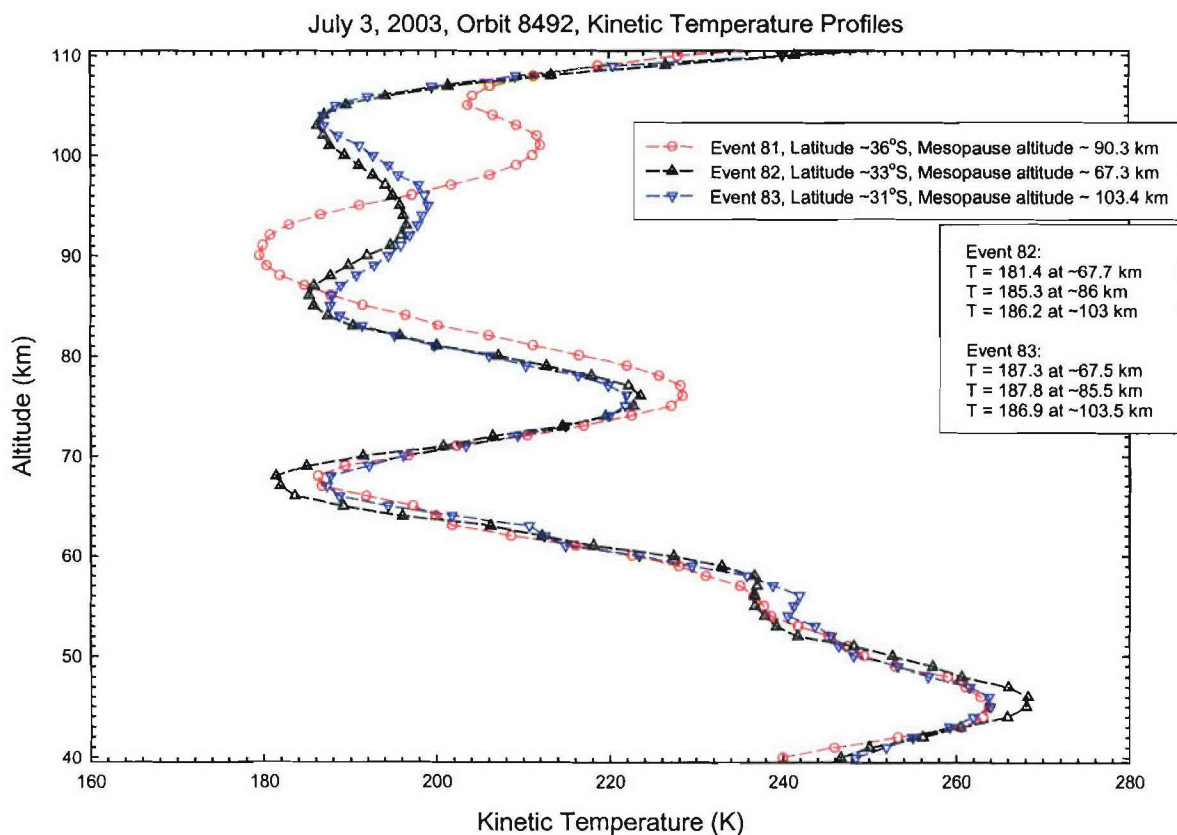
Figure 5. Temperature profiles for three successive scans on 3 July 2003. The effect of wave structure on the definition and interpretation of the mesopause altitude is apparent.
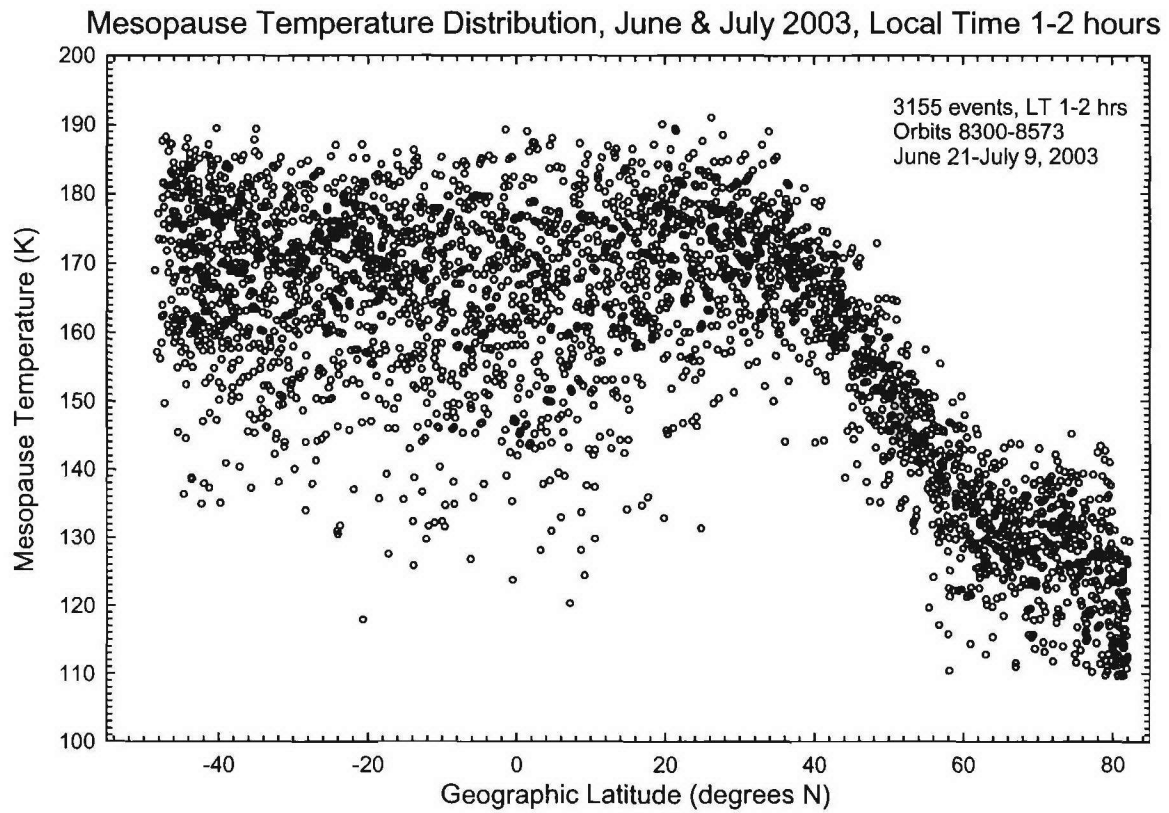
Figure 6. SABER mesopause temperature distribution for the conditions of Figure 1.
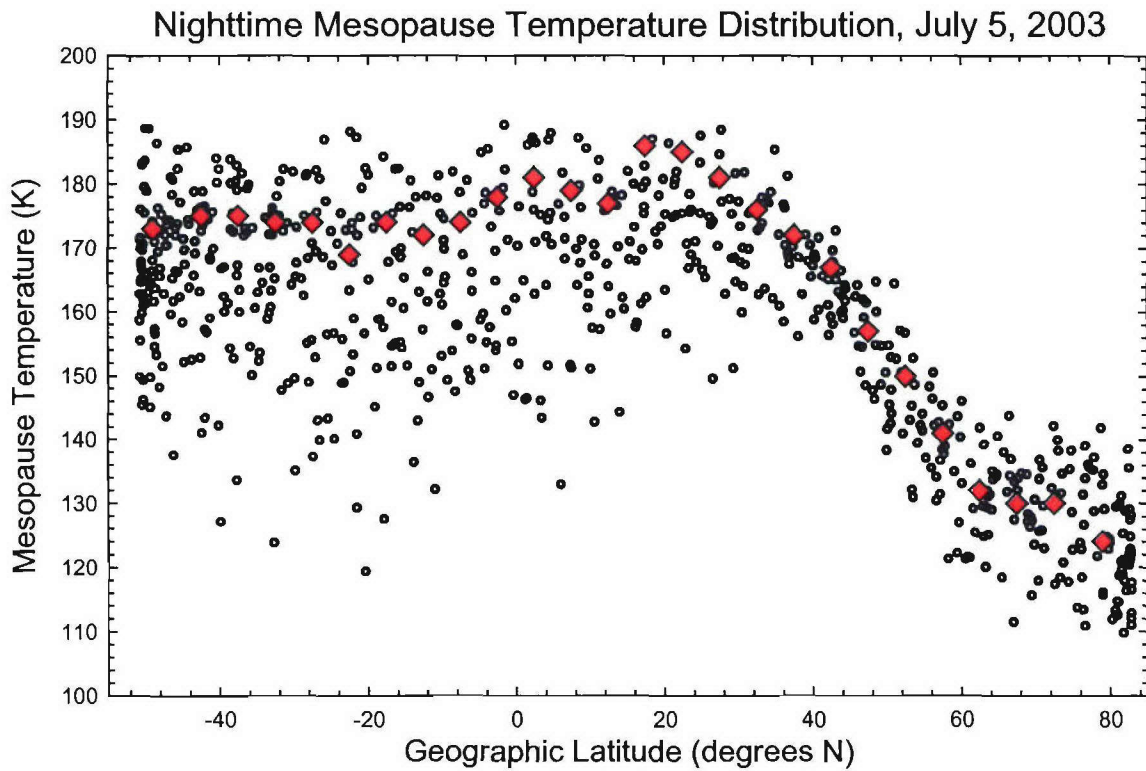
Figure 7. SABER mesopause temperature distribution for the conditions of Figure 2. Temperatures derived from mean profiles for each 5-degree latitude bin are shown in red.

Nighttime Mean Temperature Profiles, July 5, 2003

70-75°N
24 events
SZA ~ 84°
LT ~ 1.1 hrs

50-55°N
22 events
SZA ~ 102°
LT ~ 1.7 hrs

65-70°N
21 events
SZA ~ 88°
LT ~ 1.4 hrs

45-50°N
20 events
SZA ~ 106°
LT ~ 1.8 hrs

60-65°N
25 events
SZA ~ 93°
LT ~ 1.6 hrs

40-45°N
24 events
SZA ~ 110°
LT ~ 1.8 hrs

55-60°N
23 events
SZA ~ 97°
LT ~ 1.7 hrs

35-40°N
23 events
SZA ~ 115°
LT ~ 1.8 hrs

Kinetic Temperature (K)

Kinetic Temperature (K)
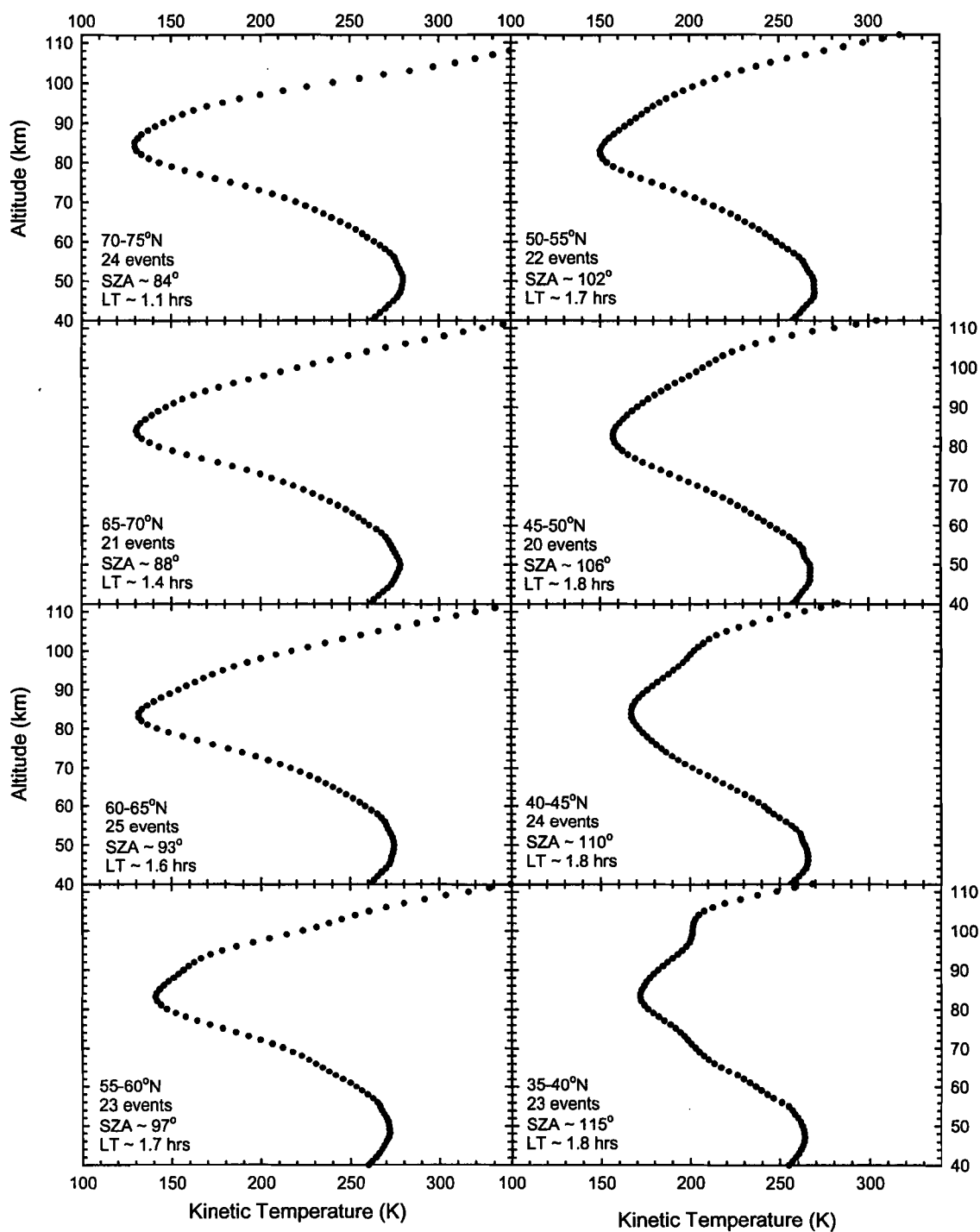
Figure 8a. Mean temperature profiles for ascending data on 5 July 2003, 5-degree latitude bins 35-75°N.

26

Nighttime Mean Temperature Profiles, July 5, 2003
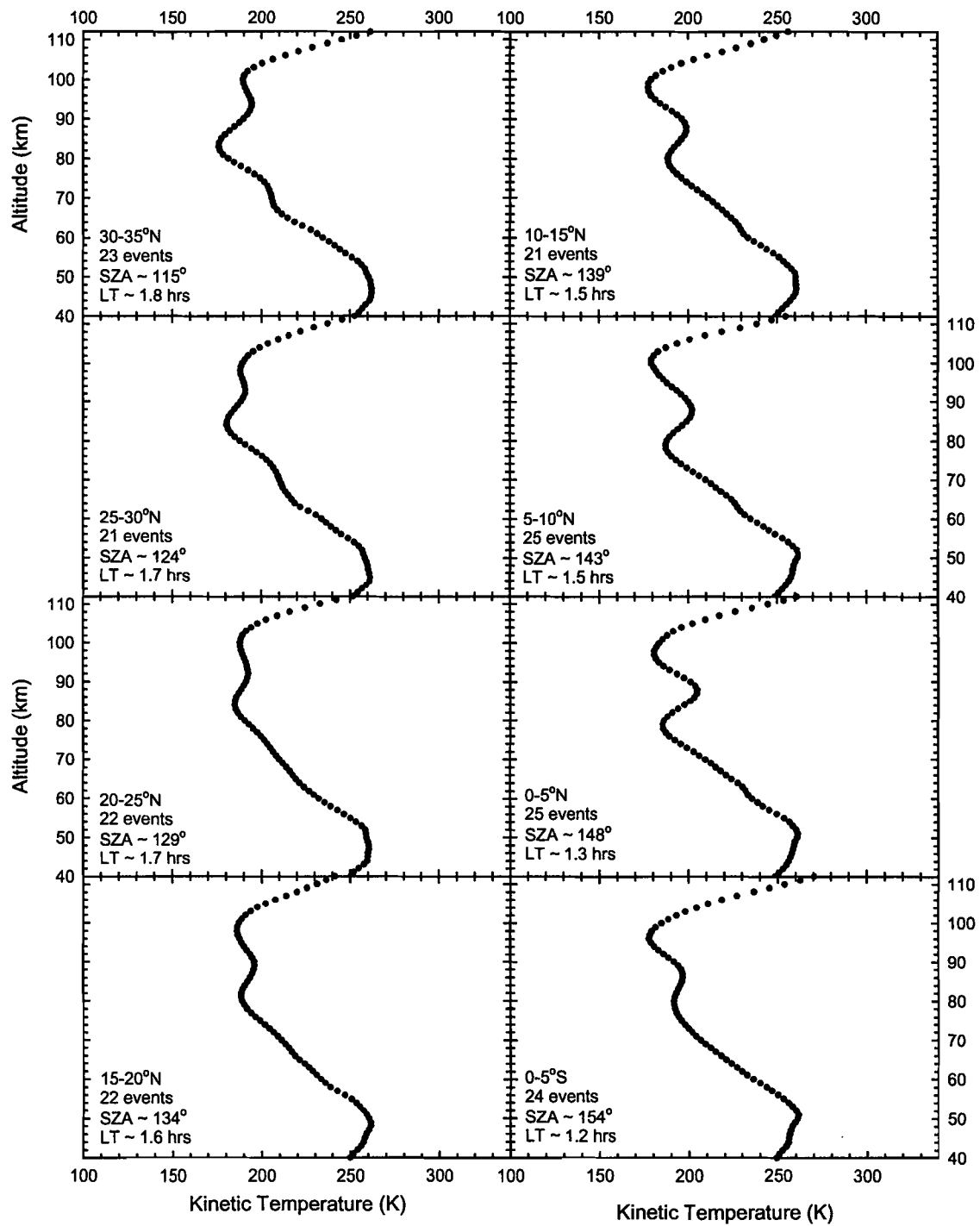
Figure 8b. As in Figure 8a, but for latitude bins 35°N-5°S.

Nighttime Mean Temperature Profiles, July 5, 2003

5-10°S
21 events
SZA ~ 159°
LT ~ 1.1 hrs

25-30°S
28 events
SZA ~ 173°
LT ~ 0.4 hrs

10-15°S
21 events
SZA ~ 164°
LT ~ 1.0 hrs

30-35°S
28 events
SZA ~ 170°
LT ~ 0.1 hrs

15-20°S
27 events
SZA ~ 168°
LT ~ 0.8 hrs

35-40°S
31 events
SZA ~ 164°
LT ~ 23.7 hrs

20-25°S
27 events
SZA ~ 172°
LT ~ 0.6 hrs

40-45°S
38 events
SZA ~ 157°
LT ~ 23.2 hrs

Kinetic Temperature (K)

Kinetic Temperature (K)
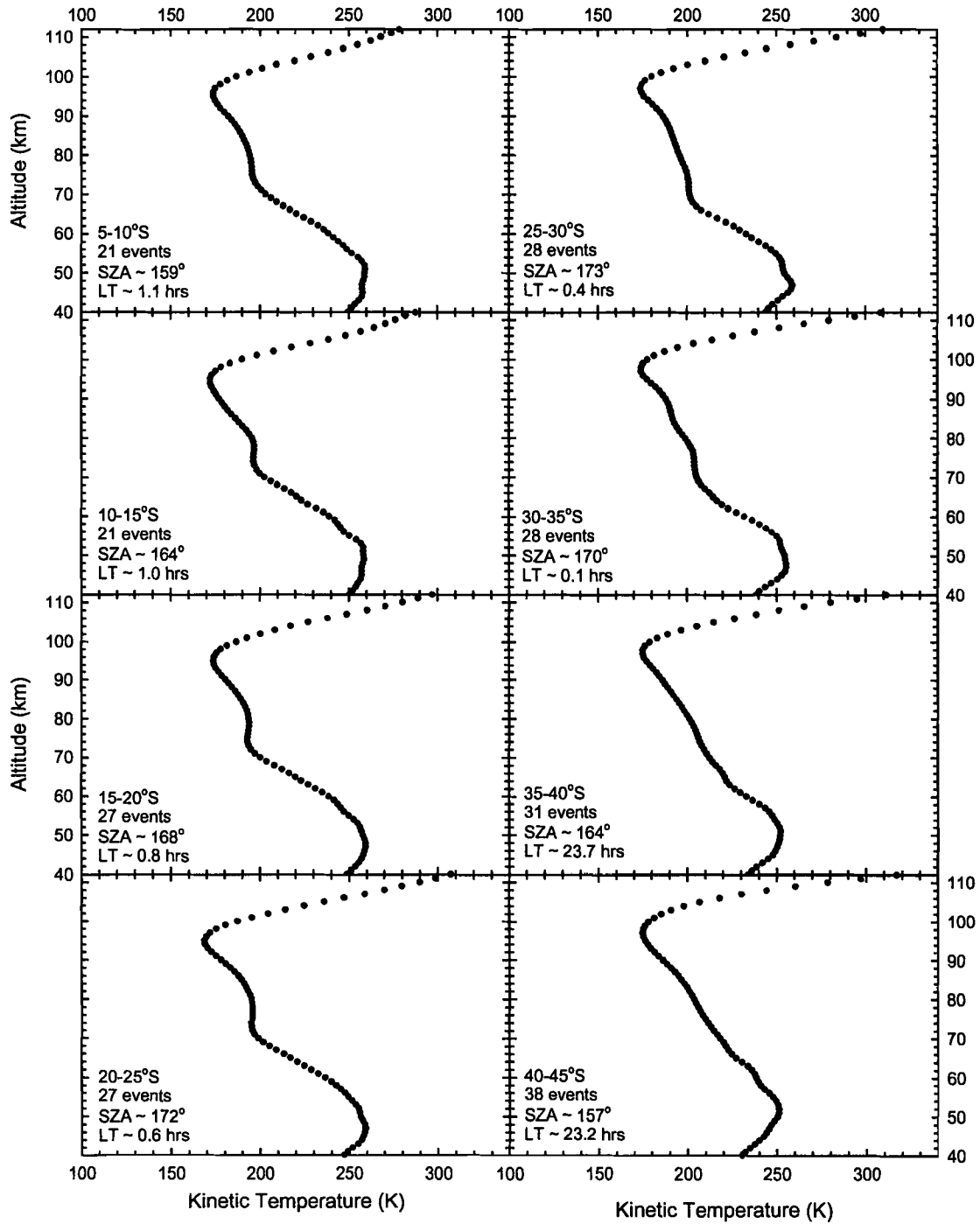
Figure 8c. As in Figure 8a, but for latitude bins 5-45°S.
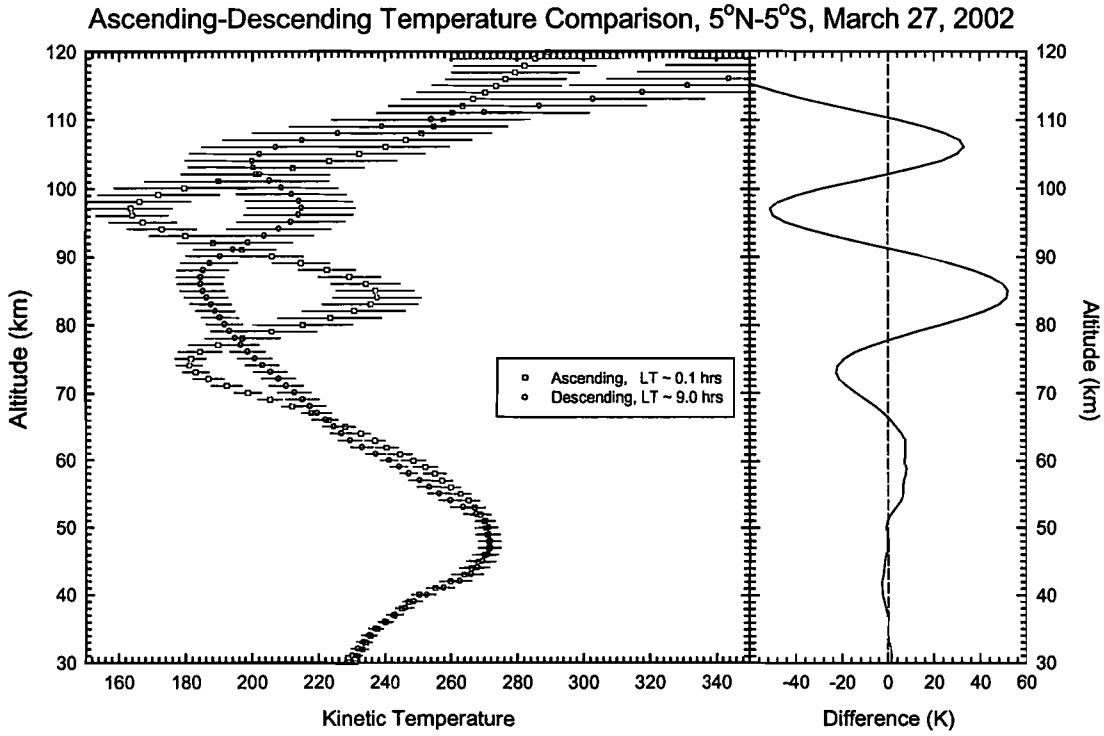
Figure 9. Comparison of mean temperature within five degrees of the equator on 27 March 2002. Profiles (left) were obtained by averaging, separately, the temperature for all events on the ascending and descending sides, for which LT~0 h and 9 h, respectively. Error bars are the rms deviations about the mean. Temperature difference (right) strongly suggests the influence of the diurnal tide.

Temperature Profiles, Orbit 1630--March 27, 2002
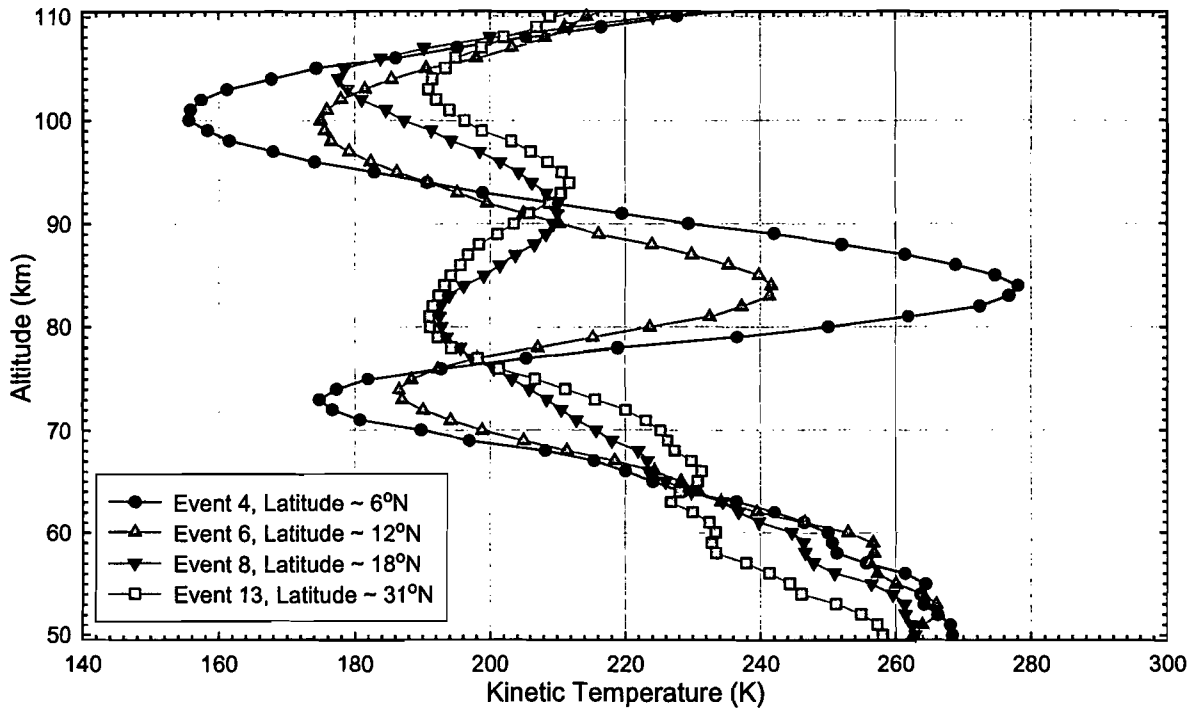
Figure 10. Four nighttime temperature profiles from 27 March 2002. TILs appear at various altitudes during each event. The largest TIL (event 4) exceeds 100 K in amplitude.

Temperature Profiles, July 13, 2002--Orbit 3218
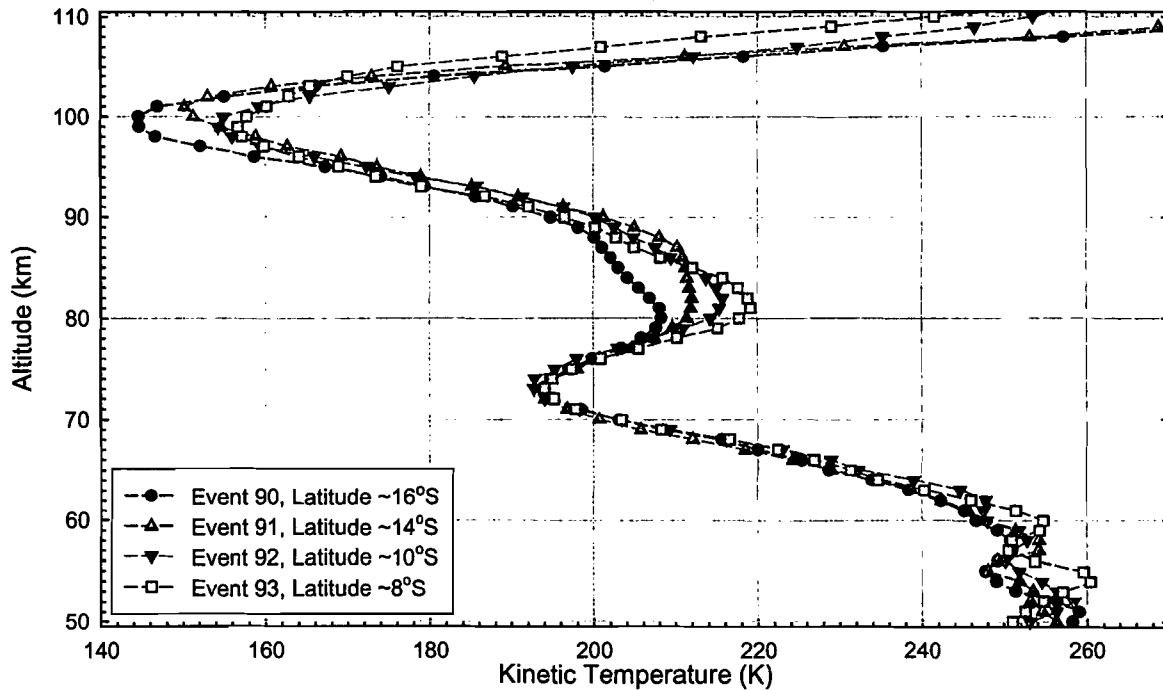
Figure 11. Four nighttime temperature profiles from July 13, 2002, from consecutive events. TILs appear at and slightly above 80 km in each case.
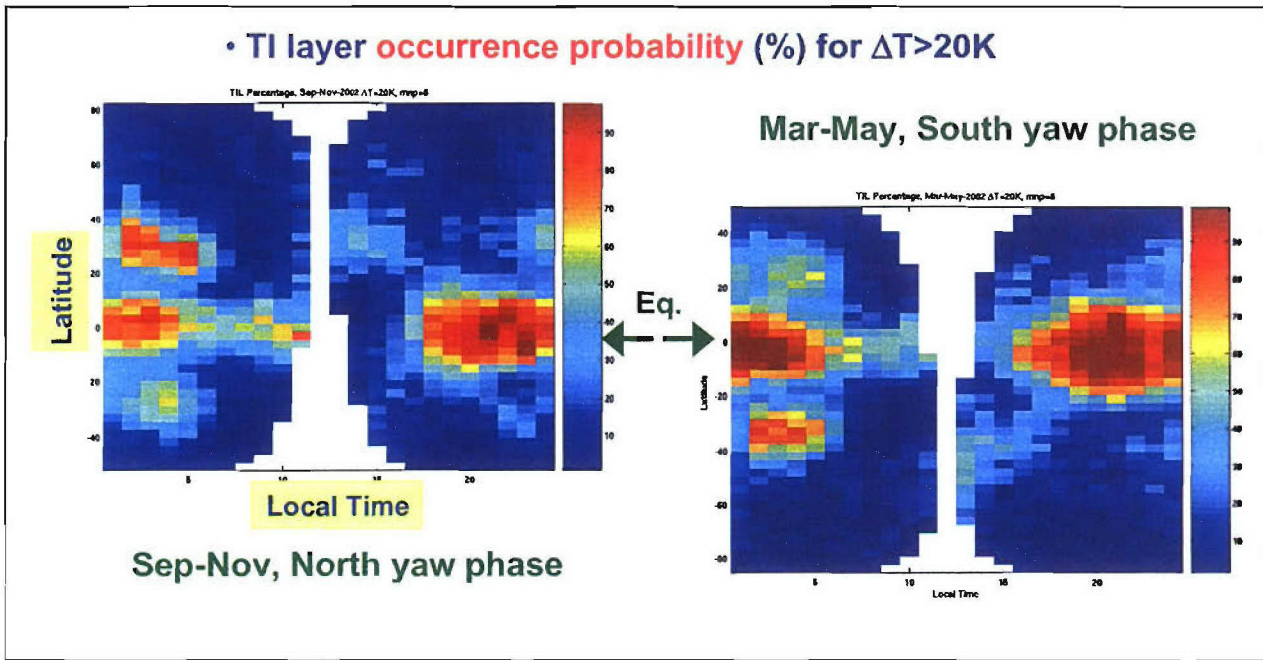
Figure 12. TIL occurrence probabilities, by latitude and local time, for two yaw cycles in 2002. In each case, the SABER data acquisition period began just at equinox. The TIL amplitude threshold was 20 K.
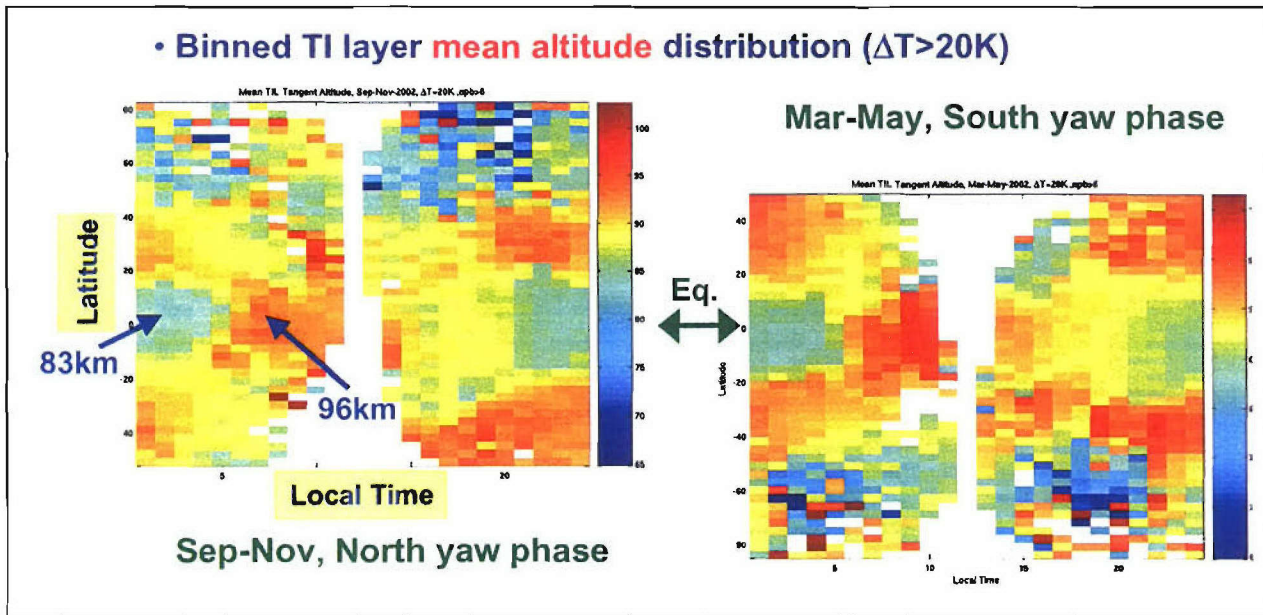
Figure 13. Mean altitude distribution of TILs, by latitude and local time, for the yaw cycles in Figure 12.
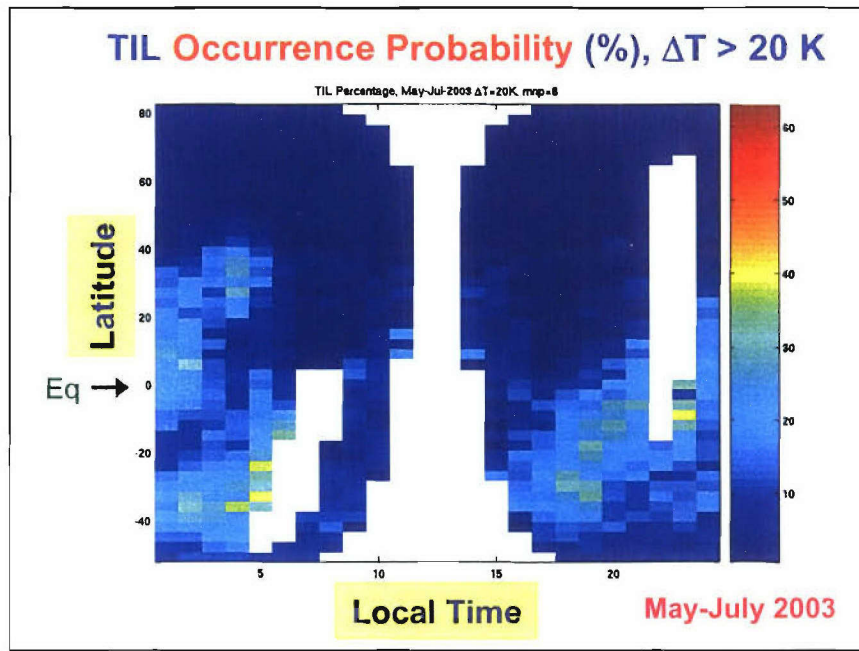
Figure 14. TIL occurrence probability, as in Figure 12 but for one yaw cycle at solstice. Northern-hemisphere summer is included. No data are available for the areas appearing in white.
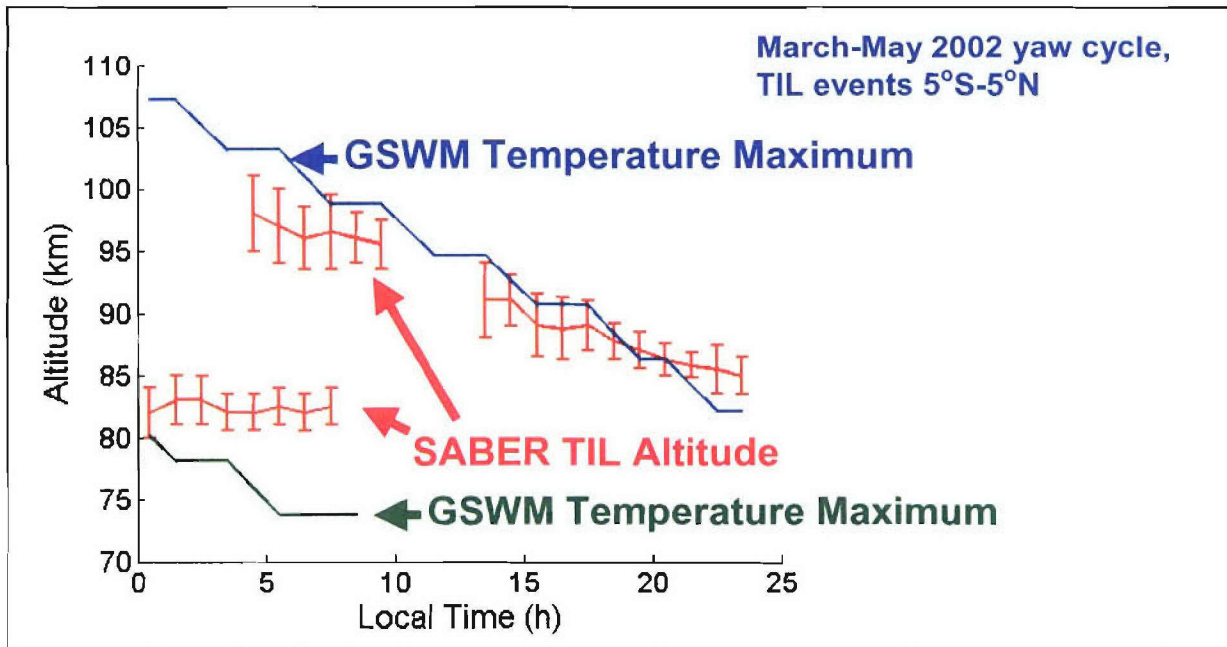
Figure 15. Mean TIL altitudes, plotted against local time, for equatorial events during March-May 2002. Also shown are the location of local tidal temperature maxima as predicted by GSWM. For higher-altitude inversions, TIL altitudes decrease with increasing local time, but lower-altitude TILs appear at approximately the same height regardless of LT.
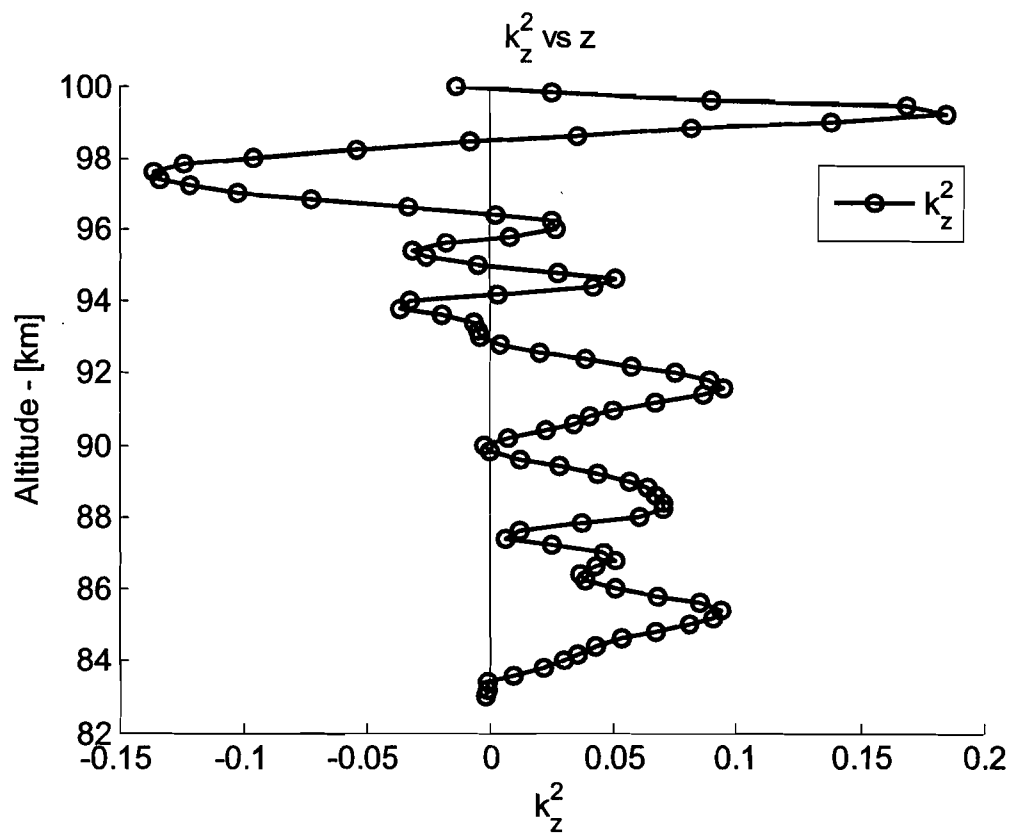
Figure 16. Helmholtz equation propagation constant (squared). Regions with positive values correspond to ducts. Background wind was smoothed with a 3-point triangle taper.

33
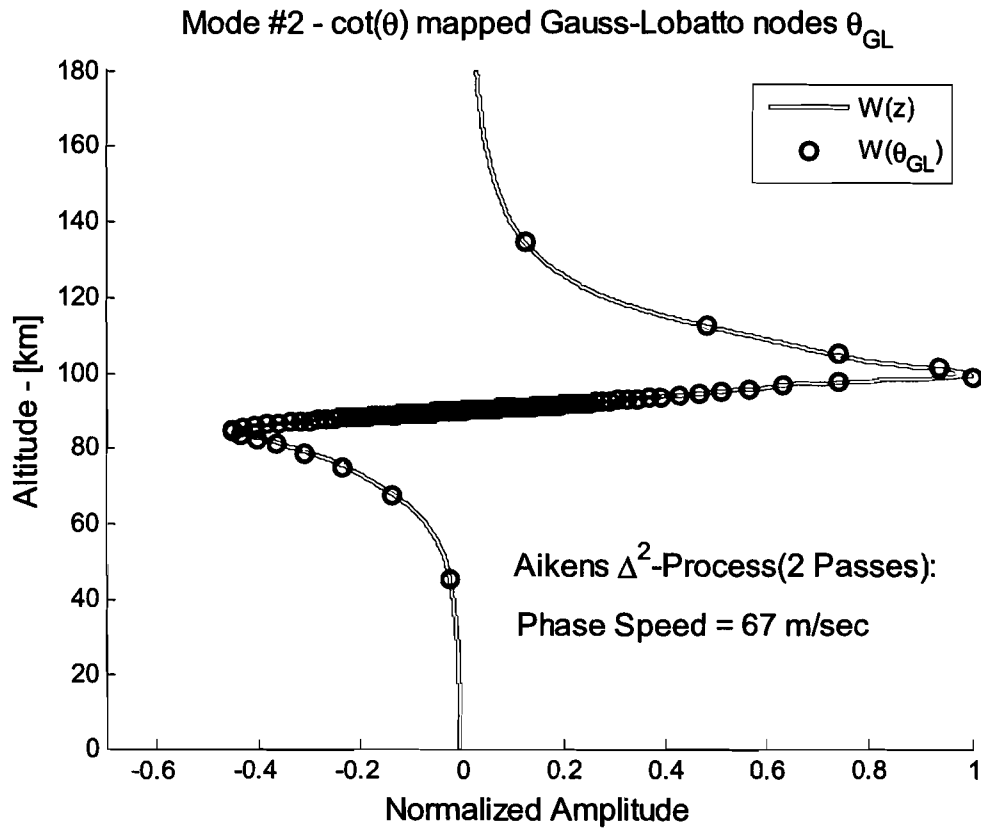
Figure 17. Helmholtz equation eigenmode #2 and phase speed, from the rational Chebyshev polynomial solution (M = 70). Background wind was smoothed with a 3-point triangle taper.
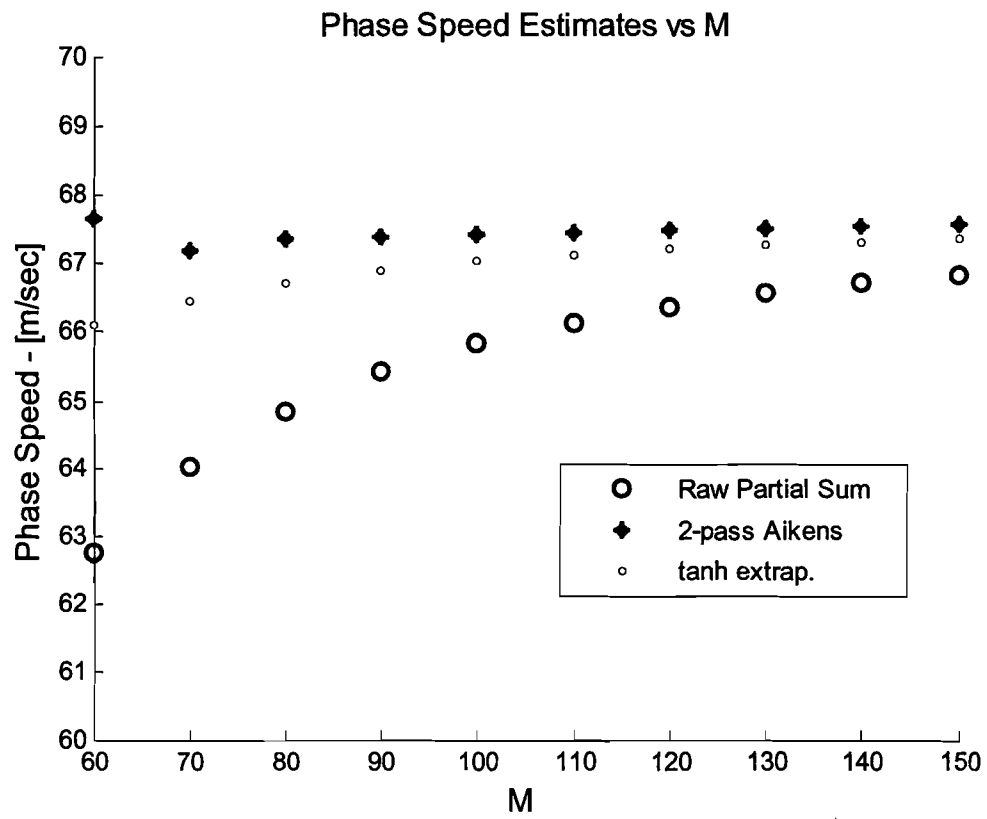
Figure 18. Convergence of phase speed estimates using rational Chebyshev polynomials.
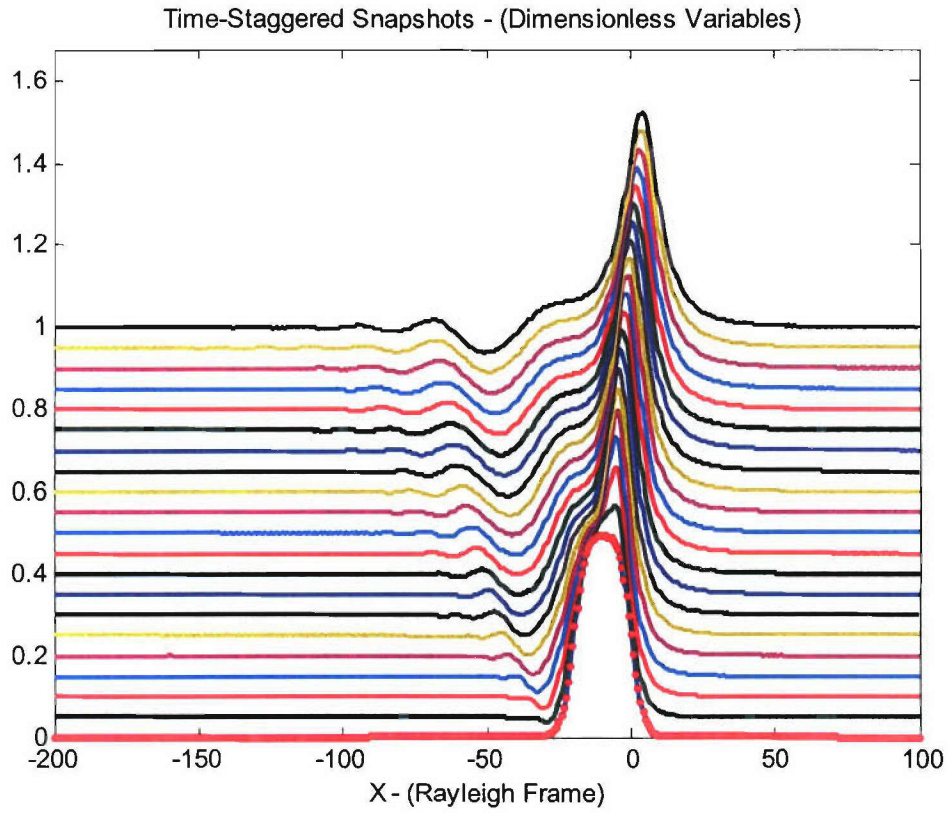
Figure 19. Solution A(X,T) of the BDOB equation. Time-staggered snapshots are shown for T = 0(5)100 in the Rayleigh frame. Initial dimensionless pulse amplitude = 0.5; eddy diffusivity related loss constant for Burgers (dimensionless) term = 0.1. Note the forward displacement of the peak for increasing T.
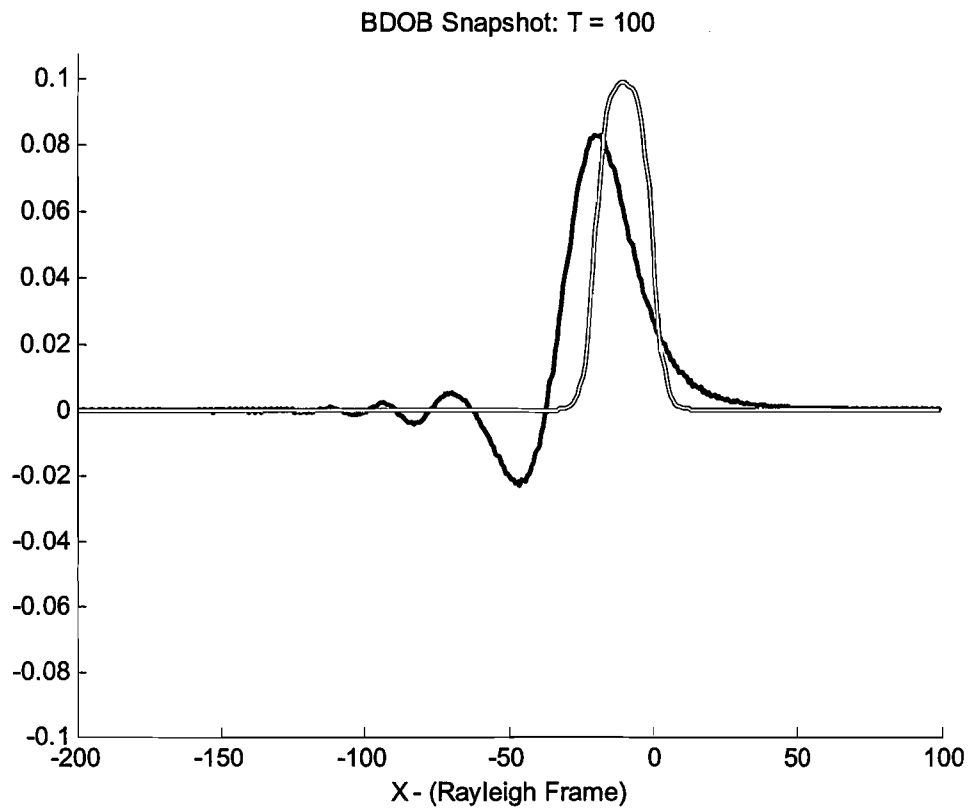
BDOB Snapshot: T = 100
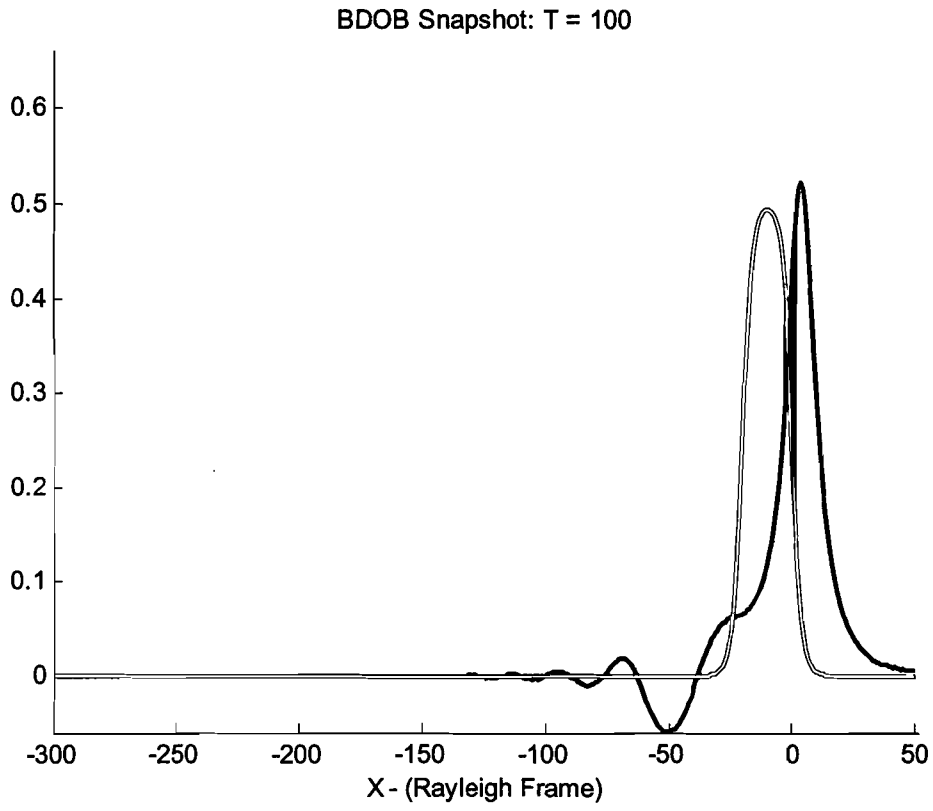
Figure 20. Snapshot of the solution $A(X, T = 0, 100)$ of the BDOB equation. Initial dimensionless pulse amplitude = 0.5; eddy diffusivity related loss constant, $\varepsilon = 0.1$. Note the forward movement of the main peak. For very large T (not shown), the peak diminishes.
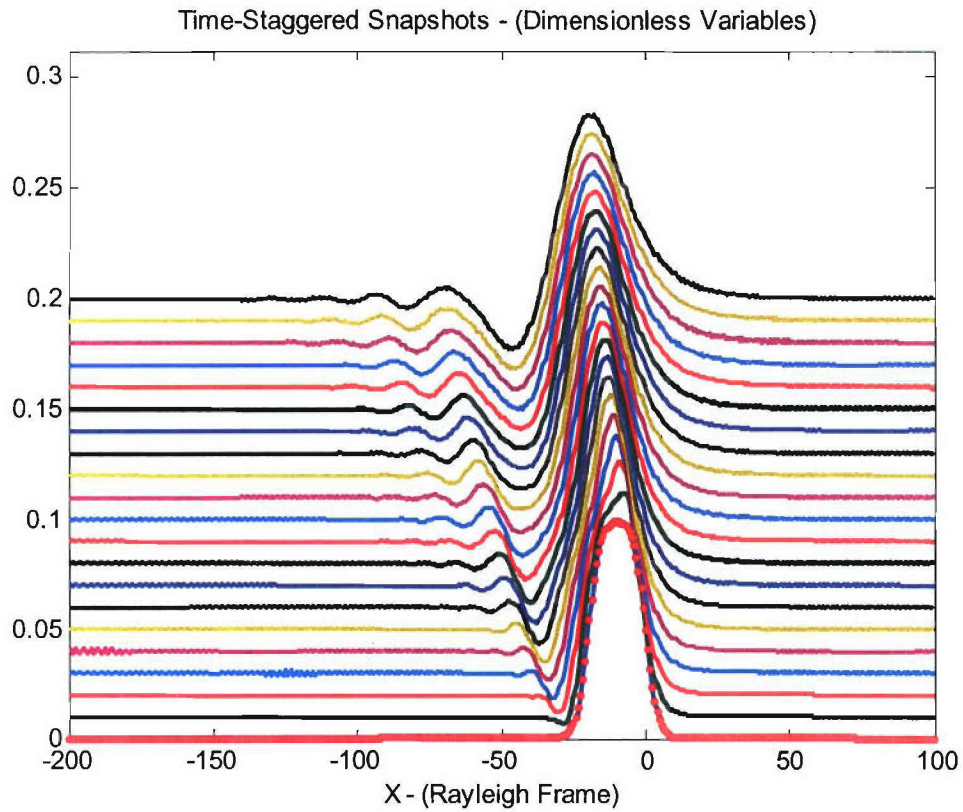
Figure 21. Time-staggered snapshots of the solution A(X,T) of the BDOB equation. Times shown are T = 0(5)100, and the solution was obtained in the Rayleigh frame. Initial dimensionless pulse amplitude = 0.1; eddy diffusivity related loss constant for the Burgers (dimensionless) term = 0.1. Note the backward displacement of the peak for increasing T.

BDOB Snapshot: T = 100

Figure 22. Snapshot of the solution $A(X, T = 0, 100)$ of the BDOB equation. Initial dimensionless pulse amplitude = 0.1; eddy diffusivity related loss constant, ε = 0.1. Note the backwards movement of the main peak. For large T (not shown), it slowly turned around and started to move forward again.
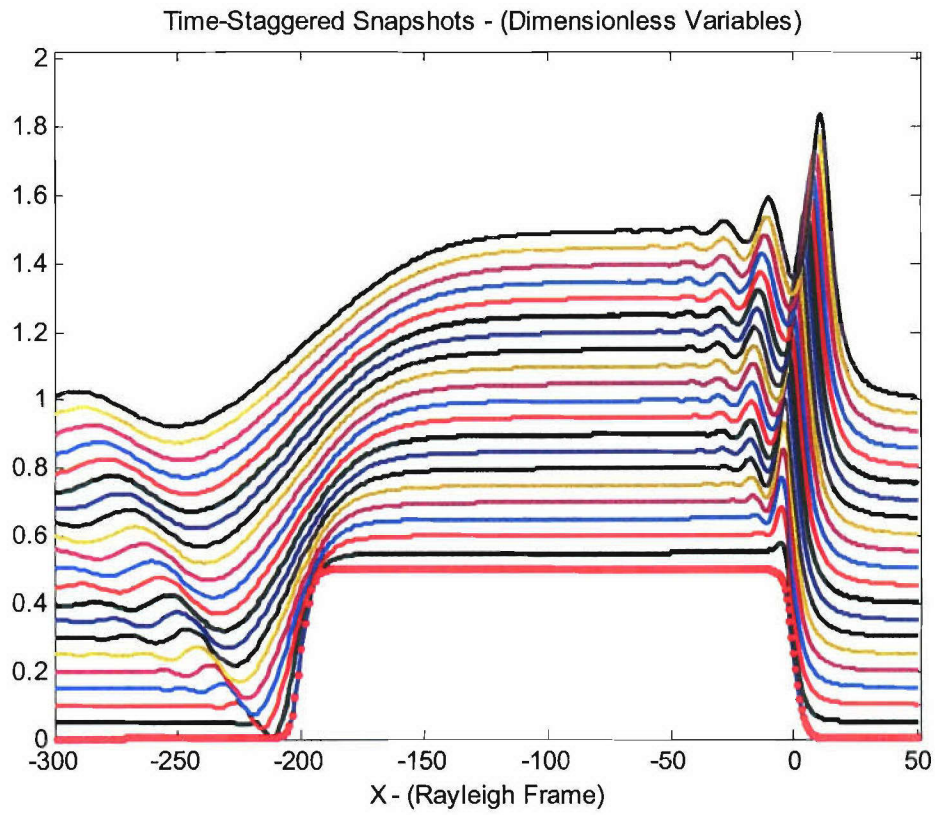
Figure 23. Solution A(X,T) of the BDOB equation assuming a very long initial pulse. Time-staggered snapshots are shown for T = 0(5)100 in the Rayleigh frame; dimensionless pulse amplitude = 0.5; eddy diffusivity Burgers (dimensionless) term = 0.1.
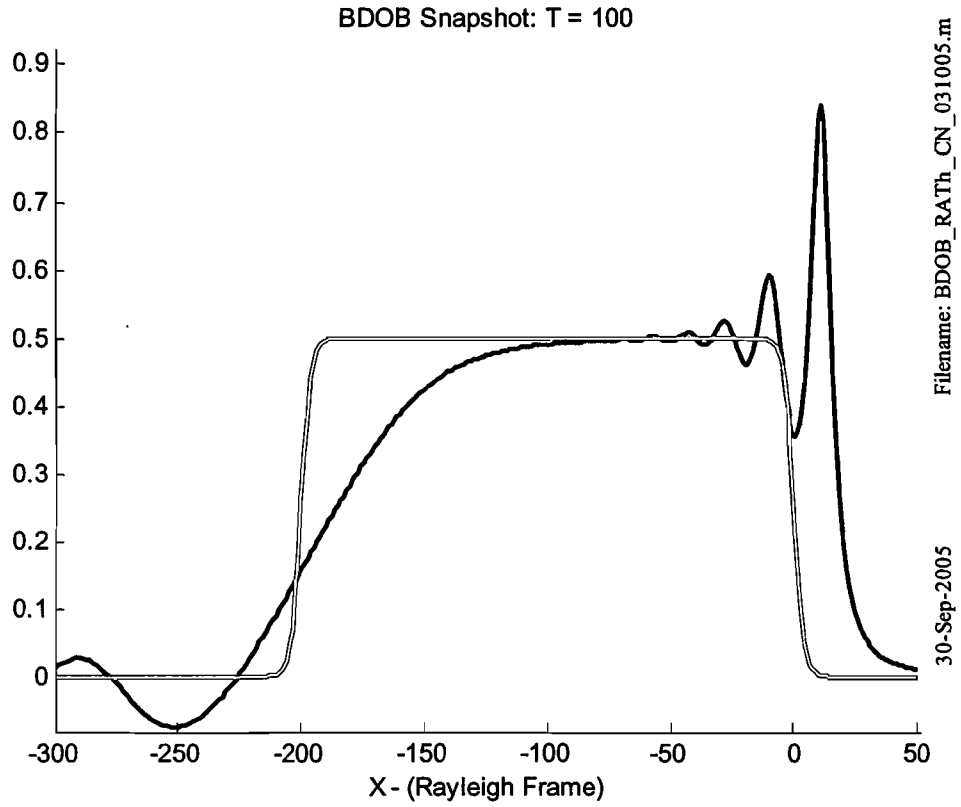
Figure 24. Snapshot of the solution $A(X, T = 0, 100)$ of the BDOB equation. Long initial dimensionless pulse amplitude = 0.5; eddy diffusivity related loss constant, $\varepsilon = 0.1$.
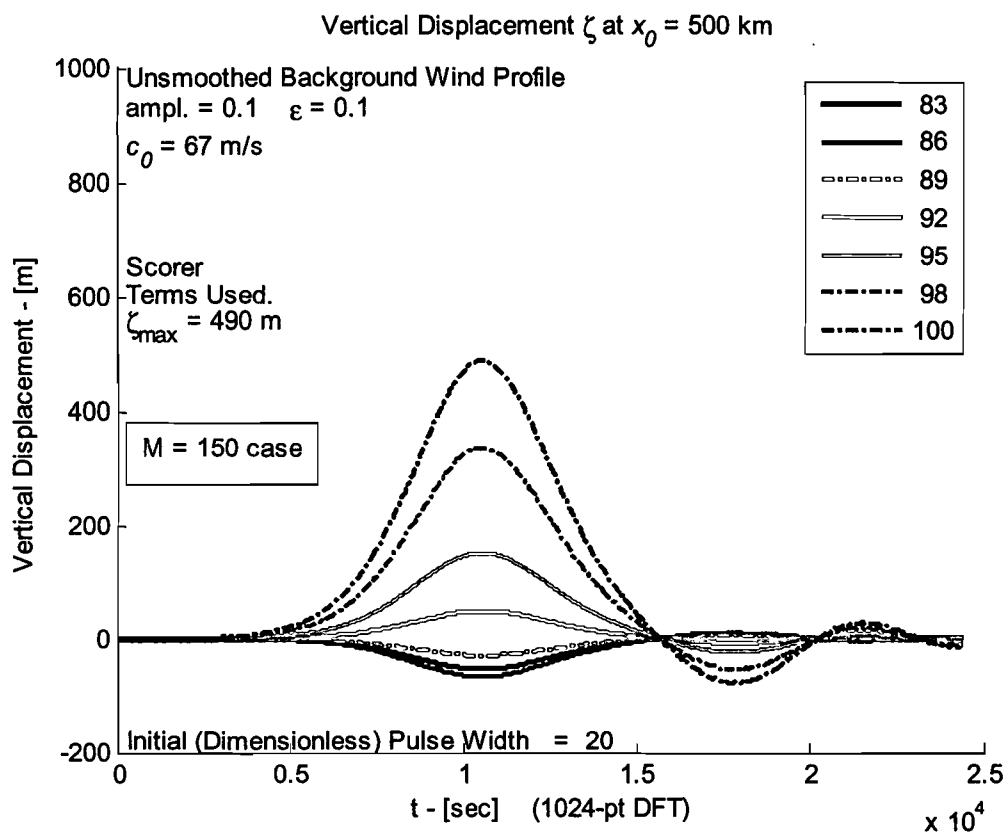
Figure 25. Evolving vertical displacements at various altitudes, from the Taylor-Goldstein and BDOB equations. No background wind smoothing was used; only Scorer terms were retained in α and β.
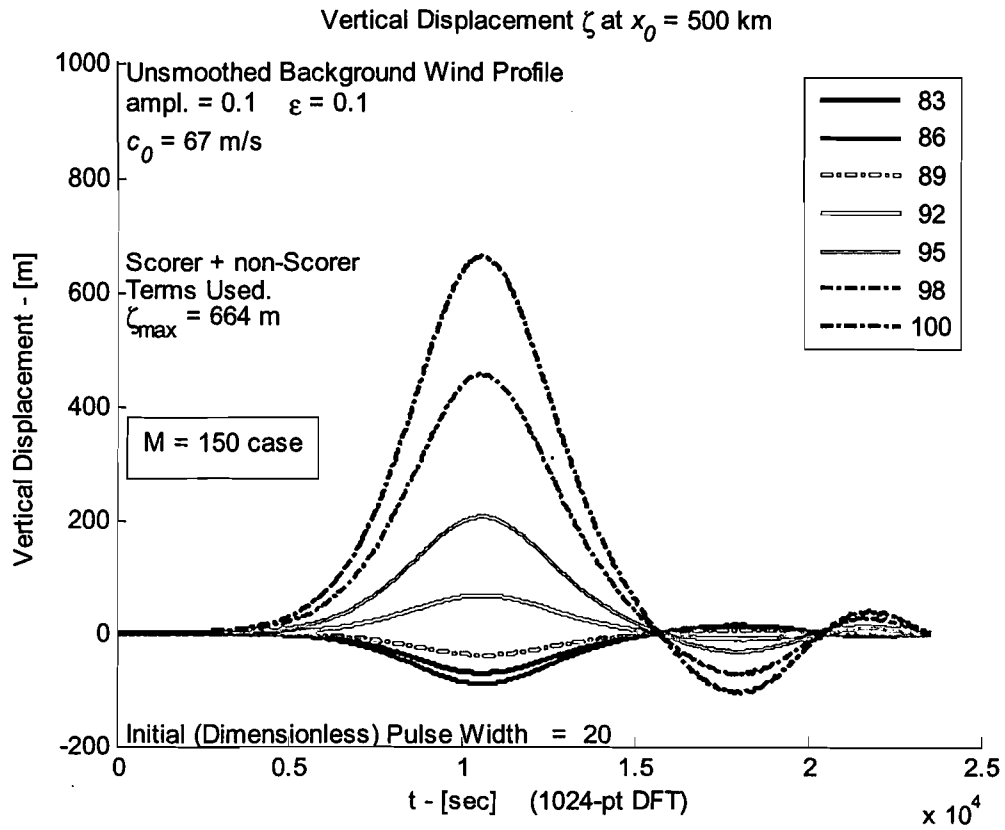
Figure 26. Evolving vertical displacements at various altitudes obtained from the Taylor-Goldstein and BDOB equations. No background wind smoothing was used; Scorer and non-Scorer terms were retained in α and β.
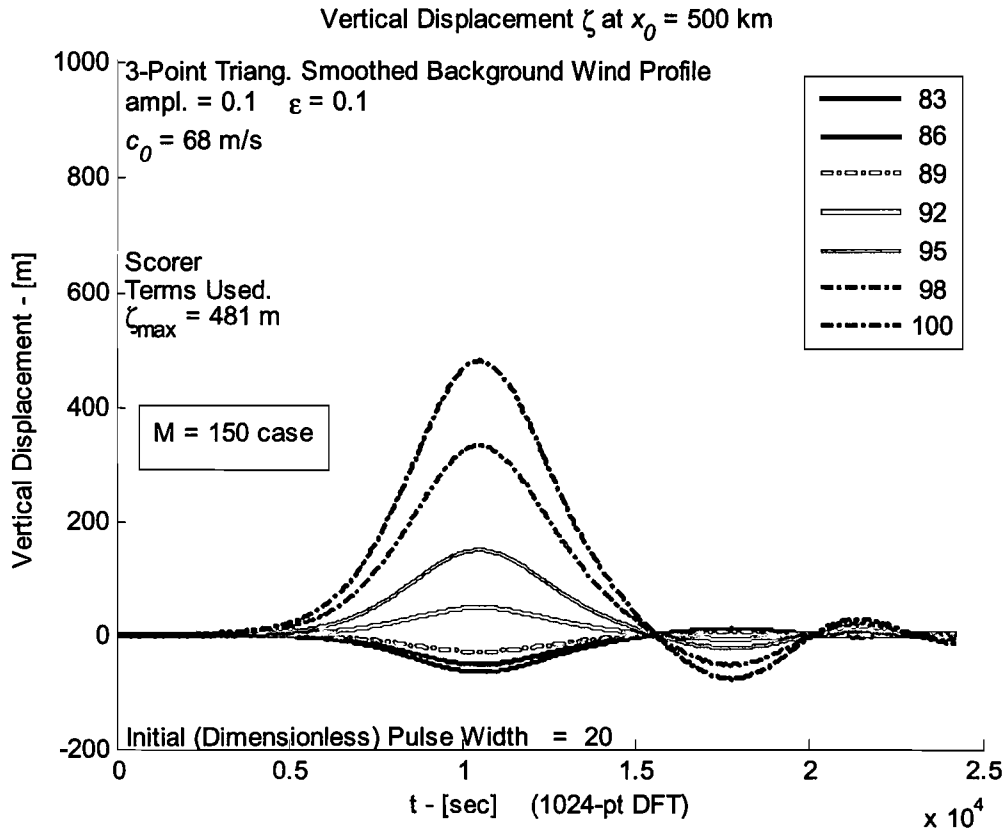
Figure 27. Evolving vertical displacements at various altitudes obtained from the Taylor-Goldstein and BDOB equations. Three-point smoothing of the background wind was used; only Scorer terms were retained in α and β.
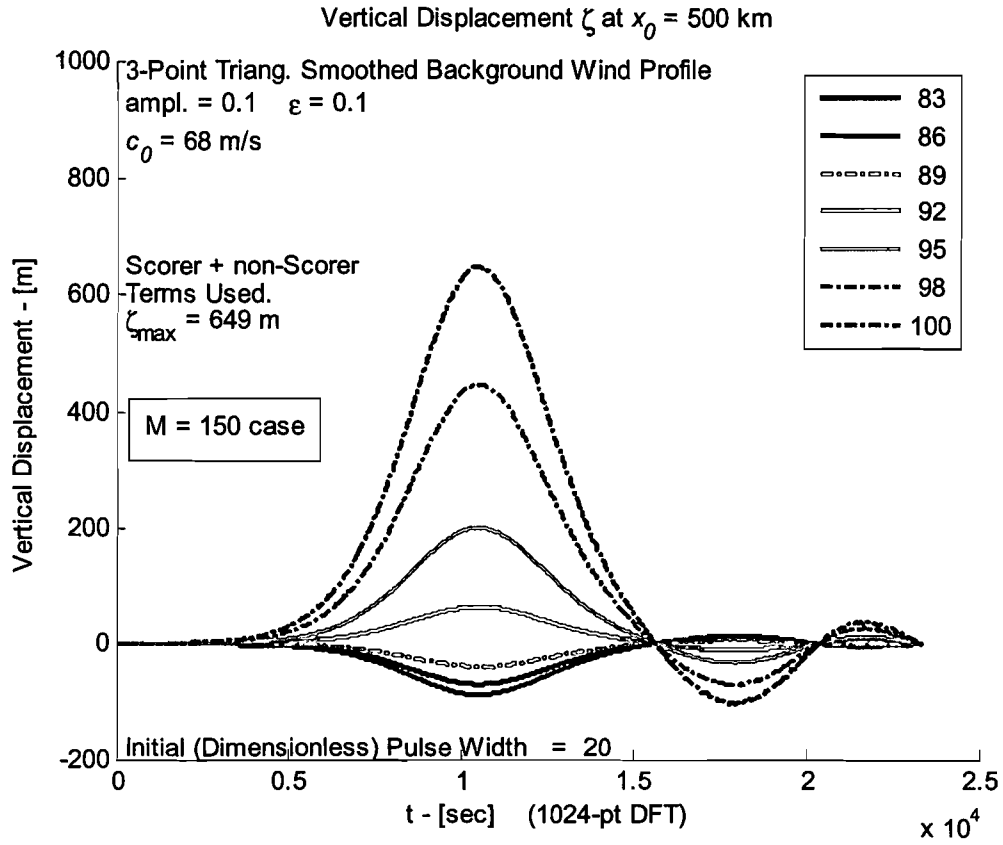
Figure 28. Evolving vertical displacements at various altitudes obtained from the Taylor-Goldstein and BDOB equations. Three-point smoothing of the background wind was used; Scorer and non-Scorer terms were retained in α and β.

45